Meteoritics & Planetary Science 37, 1651–1684 (2002)
Available online at http://www.uark.edu/meteor

Invited Review

The geology of 433 Eros

M. S. ROBINSON[1]*, P. C. THOMAS[2], J. VEVERKA[3], S. L. MURCHIE[4] AND B. B. WILCOX[5]

[1]Center for Planetary Sciences, Northwestern University, 1850 Campus Drive, Evanston, Illinois 60208, USA
[2]Center for Radiophysics and Space Research, Cornell University, Ithaca, New York 14850, USA
[3]Department of Astronomy, Cornell University, Ithaca, New York 14850, USA
[4]The John Hopkins University Applied Physics Laboratory, 11100 John Hopkins Road, Laurel, Maryland 20723, USA
[5]Hawaii Institute of Geophysics and Planetology, University of Hawaii at Manoa, Honolulu, Hawaii 96822, USA
*Correspondence author's e-mail address: robinson@earth.northwestern.edu

(Received 2002 August 9; accepted in revised form 2002 September 12)

Abstract–The global high-resolution imaging of asteroid 433 Eros by the Near-Earth Asteroid Rendezvous *(NEAR) Shoemaker* spacecraft has made it possible to develop the first comprehensive picture of the geology of a small S-type asteroid. Eros displays a variety of surface features, and evidence of a substantial regolith. Large scale facets, grooves, and ridges indicate the presence of at least one global planar structure. Directional and superposition relations of smaller structural features suggest that fracturing has occurred throughout the object. As with other small objects, impact craters dominate the overall shape as well as the small-scale topography of Eros. Depth/diameter ratios of craters on Eros average ~0.13, but the freshest craters approach lunar values of ~0.2. Ejecta block production from craters is highly variable; the majority of large blocks appear to have originated from one 7.6 km crater (Shoemaker). The interior morphology of craters does not reveal the influence of discrete mechanical boundaries at depth in the manner of craters formed on lunar mare regolith and on some parts of Phobos. This lack of mechanical boundaries, and the abundant evidence of regolith in nearly every high-resolution image, suggests a gradation in the porosity and fracturing with depth. The density of small craters is deficient at sizes below ~200 m relative to predicted slopes of empirical saturation. This characteristic, which is also found on parts of Phobos and lunar highland areas, probably results from the efficient obliteration of small craters on a body with significant topographic slopes and a thick regolith. Eros displays a variety of regolith features, such as debris aprons, fine-grained "ponded" deposits, talus cones, and bright and dark streamers on steep slopes indicative of efficient downslope movement of regolith. These processes serve to mix materials in the upper loose fragmental portion of the asteroid (regolith). In the instance of "ponded" materials and crater wall deposits, there is evidence of processes that segregate finer materials into discrete deposits. The NEAR observations have shown us that surface processes on small asteroids can be very complex and result in a wide variety of morphologic features and landforms that today seem exotic. Future missions to comets and asteroids will surely reveal still as yet unseen processes as well as give context to those discovered by the *NEAR Shoemaker* spacecraft.

INTRODUCTION

Asteroids were formed very early in the history of the solar system from materials that condensed over a range of nebular compositions and temperatures (Kerridge and Matthews, 1988; Binzel *et al.*, 1989). Large-scale differences in spectral properties among asteroids are thought to represent gross compositional differences at least partially representing radial segregation of materials in the early nebula. Subsequently asteroids experienced orbital perturbations, collisional effects, and various degrees of internal heating and differentiation (cf., Bell *et al.*, 1989 and references therein). Investigation of their formation and early history is dependent upon disentangling the effects of these various modification processes. Studying the geology of an asteroid is an attempt to determine what its physical and compositional features reveal of its history, both for that object and for possible generic application to other objects. The Near-Earth Asteroid Rendezvous (NEAR) mission to 433 Eros made a close examination of surface morphology, infrared spectra and visible colors, the mass distribution, major element chemistry of the surface, and magnetic character of this near-Earth object. This report summarizes the overall

Prelude preprint MS#4894

geology of Eros, relying mostly on images, but placed in the context of results from other instruments. The variety of geomorphic features, the presence of a substantial regolith, and the importance of local gravity on surface processes are among the characteristics that were not widely anticipated.

Eros is a highly irregular object (Fig. 1), coarsely approximated by an ellipsoid of dimensions 33 × 11 × 11 km, and has a mean radius of 8.5 km. It has a spin period of 5.27 h and a rotational obliquity of 88° (Thomas *et al.*, 2002a; Veverka *et al.*, 1999, 2000). Periapsis of the orbit is at 1.13 AU, and apoapsis at 1.73 AU (Table 1). The *NEAR Shoemaker* spacecraft entered orbit around Eros on 2000 February 14. By 2001 February 12, it had orbited Eros 230 times acquiring more than 140 000 useful images of the surface with the multispectral imager (MSI) (Hawkins *et al.*, 1997; Murchie *et al.*, 1999, 2002a; Li *et al.*, 2002; Veverka *et al.*, 1997b) with both single filter (950 nm) and multi-filter (visible–infrared) sequences. Systematic mapping was initiated from an altitude of 200 km, and provided regional coverage (typical image angular resolution ~20 m/pixel) of the then illuminated northern hemisphere. From February to July of 2000 the orbital radius was decreased in discrete steps down to 35 km before being stepped back up to 200 km by November 2000 to allow comprehensive imaging of the then illuminated southern hemisphere. While the higher altitude data provided regional coverage, the lower orbits (35–50 km) yielded high-resolution images (better than 5 m/pixel) showing surface forms in great detail. During these low orbits the irregular shape of Eros resulted in significant variations in the resolution of images. The 180° end of Eros has a radius from the center of mass as great as 17.7 km while the minimum radius to the bottom of Psyche crater is only 3.1 km, a difference in range to the spacecraft of nearly 15 km. In a 35 km orbit, this highly irregular shape resulted in differences of resolution of almost a factor of 2, from 1.7 to 3.1 m/pixel (Bussey *et al.*, 2002). In addition to studying the asteroid from low-eccentricity orbits, the *NEAR Shoemaker* spacecraft conducted a low-altitude flyover (LAF) in October 2000 when it passed within 6 km of the surface, collecting images with resolutions better than 1 m/pixel (Veverka *et al.*, 2001a; Cheng *et al.*, 2001). A series of even closer LAF was conducted in late January 2001, with the spacecraft descending to within 3 km of the surface (image resolution better than 50 cm) (Veverka *et al.*, 2001b). These maneuvers allowed the collection of ~770 images with submeter resolution. At the end of the mission the spacecraft descended to the surface, using several de-orbit burn maneuvers, landing safely on 2001 February 12 (Veverka *et al.*, 2001b). In the last phase of the descent the spacecraft acquired 68 images with resolutions between 60 cm and 1 cm/pixel (Veverka *et al.*, 2001b). Nearly the entire asteroid was imaged from 50 km orbits (~5 m/pixel), ~3% at resolutions from 1 to 2 m/pixel and ~1% at resolutions better than 1 m/pixel. The complete MSI dataset has revealed a surprisingly complex surface exhibiting a global regolith (Veverka *et al.*, 2001a) with an non-uniformly distributed population of boulders (Thomas *et al.*, 2001), a heavily cratered surface at diameters above 200 m (Veverka *et al.*, 2000; Chapman *et al.*, 2002), and grooves and ridges thought to record broad scale tectonic deformation of the asteroid (Prockter *et al.*, 2002; Thomas *et al.*, 2002b; Wilkison *et al.*, 2002).

Heavily degraded and rounded concave and convex sides (Fig. 1) dominate Eros' irregular shape. Four semi-flat facets define the convex side (centered at 270° W), while the concave

TABLE 1. Eros global properties.

Property	Value	Source
Spin pole	RA = 11.350 ± 0.02° Dec = 17.216 ± 0.02° W = 326.027° ± 1639.38864745d	Thomas *et al.* (2002a)
Obliquity	88°	Thomas *et al.* (2002a)
Volume	2535 ± 20 km^3	Thomas *et al.* (2002a)
Area	1125 ± 15 km^2	Thomas *et al.* (2002a)
Mean radius	8.46 ± 0.02 km	Thomas *et al.* (2002a)
Maximum chord	32.90 km	Thomas *et al.* (2002a)
Range of radii	3.07–17.69 km	Thomas *et al.* (2002a)
Mean density	2.64 ± 0.02 g cm^{-3}	Thomas *et al.* (2002a)
Offset of center of figure from navigation center of mass	x = –25.6 m, y = 1.6 m, z = 47.6 m	Thomas *et al.* (2002a)
Maximum slope (300 m base)	35.9°	Thomas *et al.* (2002a)
Range of dynamic heights	2.47 km (g = 0.46 cm s^{-2})	Thomas *et al.* (2002a)
Surface gravity	0.24–0.55 cm s^{-2}	Thomas *et al.* (2002a)
Surface gravity area average	0.46 cm s^{-2}	Thomas *et al.* (2002a)
Projected areas at principal axes	333, 327, 157 ± 2 km^2	Thomas *et al.* (2002a)
Geometric albedo 946 nm	0.27 ± 0.04	Clark *et al.* (2002)
estimated geometric albedo 550 nm	0.25 ± 0.05	
I/F 950 nm (normalized to incidence = 30°, emission = 0°)	0.11 ± 0.02 range (about 0.06–0.17)	Bussey *et al.* (2002)

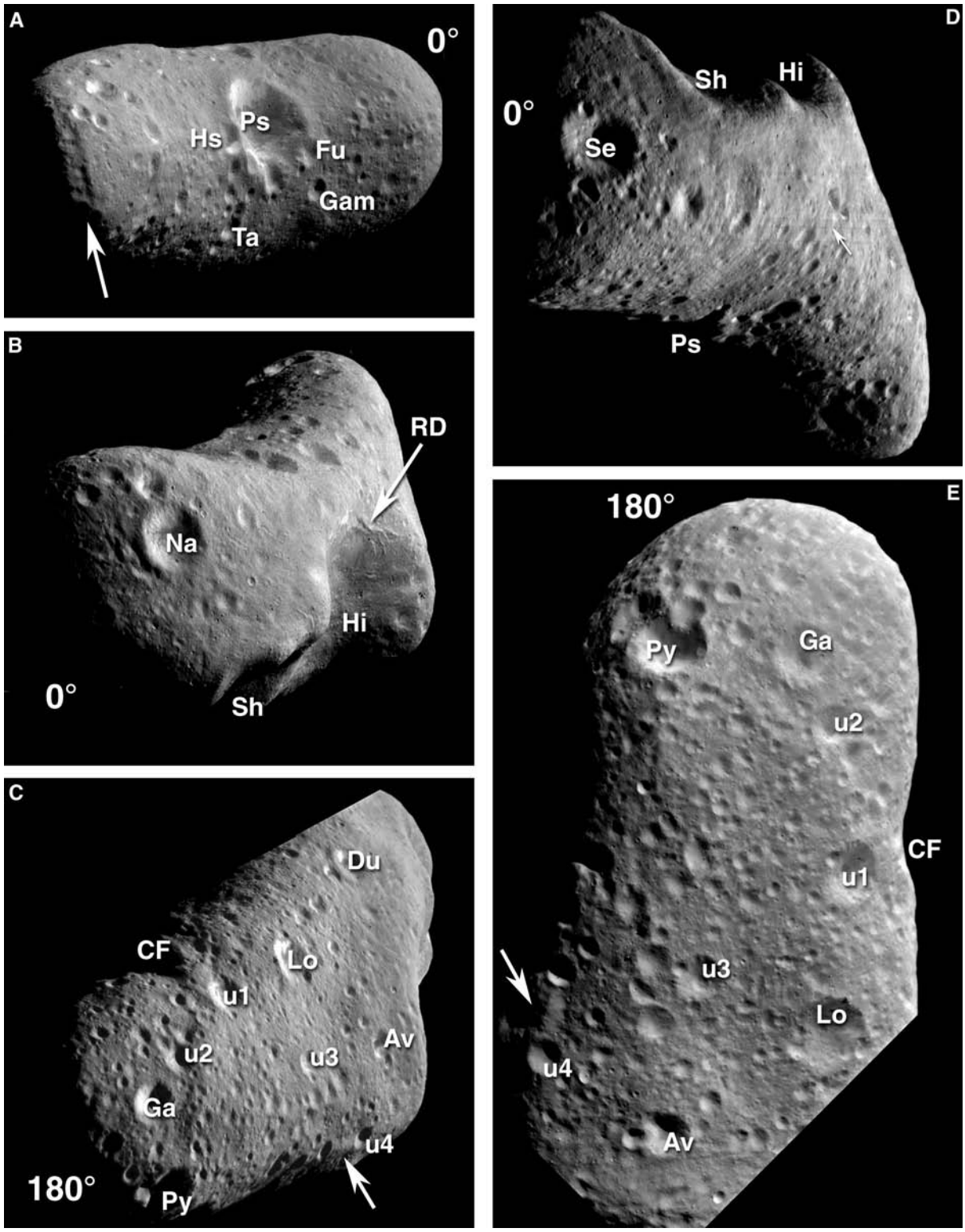

FIG. 1. Point perspective mosaics of Eros acquired while *NEAR Shoemaker* was in high orbits. See Table 2 for nomenclature. The 0° and 180° longitude notations indicate the corresponding end of the asteroid in each mosaic. For details on mosaicking procedures see Robinson *et al.* (2002a); Bussey *et al.* (2002). (a) Equatorial view centered on Psyche crater; arrow indicates trough 880 m wide by 6 km long (METs = 130663139–130663595). (b) Northern hemisphere view, arrow labeled "RD" indicates termination trough of Rahe Dorsum (METs = 127389116–127390340). (c) Southern hemisphere view from 180° end of asteroid; arrow indicates prominent unnamed ridge (see also panel (e) (METs = 144716832–144717762). (d) Southern hemisphere view from 0° end of asteroid, south pole indicated with arrow (METs = 148144333–148145015). (e) Near normal view of southern hemisphere; arrow indicates the same unnamed ridge seen in panel (c) (METs = 146150232–146151100).

side (centered at 90° W) is composed of a single curved surface. Ground-based radar studies (Mitchell *et al.*, 1998) obtained a fairly accurate shape and pole position, showing that Eros was somewhat curved, and the shape is indeed now described as banana-like, when viewed from the north or south pole directions. The radius of curvature of the surface on the concave side is roughly 29 km. A line down the center of a cross section of the asteroid viewed from the poles also has a radius of curvature of ~29 km. An arc of a circle does not easily fit the convex side. These fit shapes are of a limb and an arbitrary centerline. No smooth surfaces show this form, and structural patterns do not follow this curve. It is impossible to relate this curvature to any former structure, and we do not interpret it as other than the net effect of removal and redistribution of material by impacts. On the convex side are the ~11 km diameter crater Himeros and the ~7 km diameter crater Shoemaker (names used within this paper follow published usage since NEAR's orbital insertion; official IAU names differ in two instances from those used here: Shoemaker crater *vs.* Charlois crater, and Rahe Dorsum *vs.* Hinks Dorsum), containing Shoemaker Regio, that overlaps the western margin of Himeros. On the concave side is the relatively well-defined 5.3 km diameter crater Psyche (Veverka *et al.*, 2000; Thomas *et al.*, 2002a). At the next level of detail (1 km to 100 m), Eros is marked by a series of groove and ridge patterns that show many orientations superposed on a heavily cratered surface (Veverka *et al.*, 2000, 2001a; Prockter *et al.*, 2002; Thomas *et al.*, 2002b). Finally, at the <50 m scale the asteroid morphology is dominated by boulders and other features indicative of regolith accumulation and transport. At all scales the majority of surface features are rounded or infilled, a condition that suggests a steady erosion and comminution of surface materials resulting in a global covering of loose fragmental debris—a regolith.

Preliminary analyses of the color properties of Eros measured by the MSI are presented in Robinson *et al.* (2001) and Murchie *et al.* (2002b). Murchie *et al.* (2002b) raised four major questions. (1) Are there large-scale color heterogeneities and what are their magnitude and spatial distribution? (2) Do albedo and color units on Eros appear similar or dissimilar to those found on Gaspra, Ida, and the Moon? (3) Can evidence be found for similar or different processes affecting these bodies' color and albedo properties? (4) What clues about regolith processes on Eros do the high-resolution multispectral imaging (better than 5 m/pixel angular resolution) reveal?

At the time of the Murchie *et al.* (2002b) study only half the asteroid had been imaged; thus, their investigation was limited to approach images and early orbital color of the northern hemisphere. From these restricted data several key observations were made. Despite strong reflectance variations (2×), color variations were relatively small (*i.e.*, <10% in the 950/760 nm ratio) thus distinguishing Eros from the Main Belt S-asteroids Gaspra and Ida and from the lunar maria (Carr *et al.*, 1994; Geissler *et al.*, 1996; Sullivan *et al.*, 1996). Concentrations of discrete higher reflectance patches were found associated with steep slopes within large craters (see also Clark *et al.*, 2001; Thomas *et al.*, 2002a), a type of feature not yet observed on other small bodies. The sharpness of the boundaries of these albedo patches distinguishes them from the diffuse downslope edges of bright albedo patches found on Deimos (Thomas, 1979). Finally, on Eros high-albedo and relatively blue ejecta patterns are not found around small craters, while such features are found on the Main Belt S asteroids (Gaspra and Ida), Phobos and Deimos, and the lunar maria (Wilhelms, 1987; Carr *et al.*, 1994; Sullivan *et al.*, 1996; Pieters *et al.*, 2001). Additionally, it was noted by Murchie *et al.* (2002b) that on Eros there is a measurable dependence of the 950 to 750 nm ratio with incidence angle—materials appear "redder" at higher incidence angles, a common characteristic of silicate powders measured in the laboratory (Gradie *et al.*, 1980; Gradie and Veverka, 1986).

Analysis of a sampling of high spatial resolution color observations revealed a class of smooth deposits ("ponded deposits" or "ponds") that have color properties unambiguously distinct from the surrounding terrain (Robinson *et al.*, 2001). The ponds are relatively blue (high 550/760 nm reflectance ratios) in the visible wavelength range and have a deeper 1 μm mafic band (interpreted to be due to absorption by olivine and pyroxene as indicated by 950/760 nm ratios). The ponds also exhibit a somewhat elevated reflectance at 750 nm relative to their surroundings (<5%). To date all analysis of *NEAR Shoemaker* remote sensing measurements (gamma-ray spectroscopy (GRS), magnetometer (MAG), MSI, near-infrared spectroscopy (NIS), x-ray spectroscopy (XRS)) of the asteroid imply a compositionally homogeneous body (Acuna *et al.*, 2002; Bell *et al.*, 2002; Murchie *et al.*, 2002b; Evans *et al.*, 2001; McCoy *et al.*, 2001, 2002; Nittler *et al.*, 2001; Trombka *et al.*, 2001; Domingue *et al.*, 2002; Lucey *et al.*, 2002) discounting the possibility that the pond color properties indicate exposures of a different rock type. Alternative explanations for these color differences include secondary alteration (space weathering), mineral sorting, or differences in grain size (see discussion below). In summary, two classes of color anomalies have been identified on Eros: high-albedo deposits found on steeply sloping facets, and horizontal smooth deposits known as ponds. No color anomalies indicative of bedrock outcrops have been identified.

STRATIGRAPHIC RELATIONS

The largest feature identifiable on Eros is Himeros (11 km average diameter; Fig. 2 and Table 2). It is a roughly equi-dimensional, bowl-shaped depression ~1.5 km in depth, with a distinct raised rim on parts of its perimeter visible in images acquired with grazing incidence and evident in the image-based and laser-based shape models (Thomas *et al.*, 2002a; Zuber *et al.*, 2000). These characteristics suggest strongly that Himeros is an impact crater. Its size relative to Eros is consistent with crater sizes predicted to be able to form (Asphaug and Melosh,

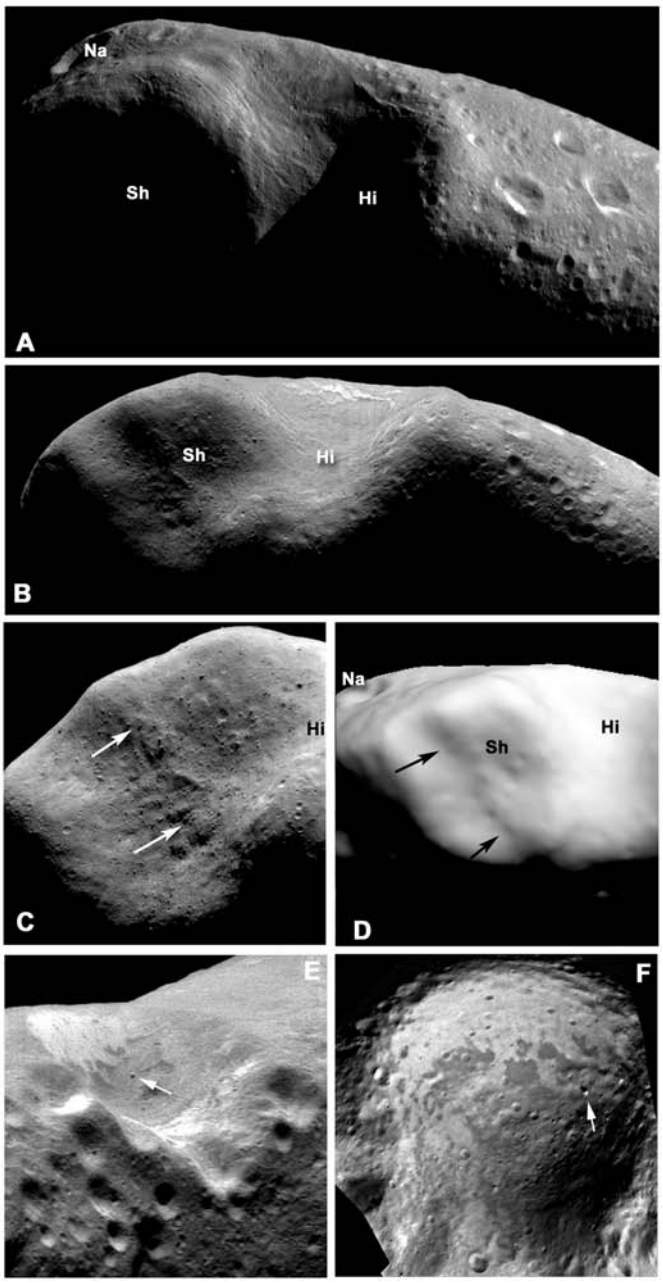

FIG. 2. The overall elongate shape of Eros is superposed by three major impact features: Himeros (Hi) crater (~11 km diameter; (a) and (b)), Shoemaker (Sh) crater (~7 km diameter; (b), (c), and (d)), and Psyche (Ps) crater (~5.3 km diameter; (e) and (f), arrows indicate same boulder). Panel (d) is a shaded relief image created from the image-based shape model of Thomas *et al.* (2002a). Panels (c) and (d) show approximately the same areas of the asteroid, centered on Shoemaker crater; the arrows indicate the rough hummocky ridge that is aligned with segments of Himeros crater's rim (METs (a) = 127520736–127521356; (b) = 127734289–127734475; (c) = 130275515N130275899; (e) = 127705784–127705970; (f) = 143963632–143963818).

1993) and observed (Thomas, 1999; Veverka *et al.*, 1997a) on small solar system bodies. Himeros's slightly elongate shape is probably due to wall failure as the crater exceeded the radius of the asteroid in the north–south direction. The interior of Himeros contains exposed scarps, slump materials, albedo streamers, and boulders: evidence that the interior has been resurfaced and modified since the formation of the initial crater cavity.

Shoemaker crater (Fig. 2) is 7 km in diameter, several hundred meters deep, and is superposed on the southwest rim of Himeros (showing Shoemaker crater to be younger). Like those of Himeros, a rounded and smooth raised rim marks Shoemaker crater's margins. The interior of Shoemaker has relatively few craters and is covered with boulders, slumps, and what appears to be a relatively thick and unconsolidated layer of regolith—this blanketing material has been termed Shoemaker Regio. Similar to Himeros, Shoemaker crater is large enough relative to the asteroid that its walls probably also failed during crater growth resulting in its low depth-to-diameter ratio (*d/D* of 0.12; see discussion below) and smoothed rim. Shoemaker crater appears very segmented and irregular in outline (Fig. 2) depending on lighting and viewing geometry. However, some of its departure from a simple, round bowl form may be due to the underlying topography. The southwest and northwest rims of Shoemaker appear to be influenced by the two facets of Eros' shape to the west of the crater (Fig. 2c especially) (see also Thomas *et al.*, 2002b). A curving ridge traverses much of the interior of Shoemaker and gives the visual impression (Fig. 2d) of aligning with the rim of Himeros. It is not obvious how such preexisting topography or strength discontinuities might affect the shape of the crater cavity.

The third largest impact crater on Eros is Psyche (5.3 km diameter and depth of ~1 km; Fig. 2). The relative ages of Psyche crater and Himeros crater are not clear. Psyche exhibits the freshest morphology; however, its southern rim may be cut by up to four 1 km craters: the highest population of superposed 1 km or larger craters on any of the three large craters (Fig. 3). However, since the area of Psyche is small, the crater counts are statistically unreliable. Both Psyche and Himeros have about the same crater densities, although these may be strongly affected by slope processes (resurfacing—see below). Results of modeling ejecta patterns from Shoemaker crater and the actual distribution of boulders (ejecta) inside Psyche indicate that Psyche is older than Shoemaker (Thomas *et al.*, 2001).

The three largest craters on Eros are all characterized by smoothed rims, superposed craters, and resurfaced interiors—evidence that all three features are relatively old. Superposition relations and ejecta patterns show that Shoemaker crater is the youngest of the three; however, the age relations between Himeros and Psyche remain ambiguous. The interior morphology of all three craters is dominated by regolith features that are discussed in detail in other sections.

TABLE 2. Feature names on Eros, abbreviations used on figures to indicate feature names.

Abbreviation	Name	Latitude	Longitude	Diameter (km)
Av	Avtandil	22.5° S	233.1° W	1.2
CF	Calisto Fossae	25° S	165° W	n/a
Du	Dulcinea	76.1° S	272.9° W	1.4
Fu	Fujitsubo	3.8° S	62.7° W	1.7
Ga	Galatea	10.2° S	183.1° W	1.4
Gam	Gamba	20.6° S	54.1° W	1.3
Hi	Himeros	21° N	282° W	11.1
Hs	Hios	9.4° S	130.9° W	1.3
Lo	Lolita	35.2° S	197.7° W	1.8
Na	Narcissus	18.2° N	7.1° W	2.9
Ps	Psyche	32° N	94° W	5.3
Py	Pygmalion	1.9° S	191.9° W	1.8
Se	Selene	14.2° S	12.5° W	3.6
Ta	Tai-yu	47.0° S	126.1° W	1.4
Sh	Shoemaker	16° S	330° W	7.6
u1	–	23.94° S	185.25° W	1.62
u2	–	14.84° S	183.18° W	1.19
u3	–	18.25° S	209.21° W	1.15
u4	–	4.31° S	229.52° W	0.86

Abbreviations: n/a = not applicable.

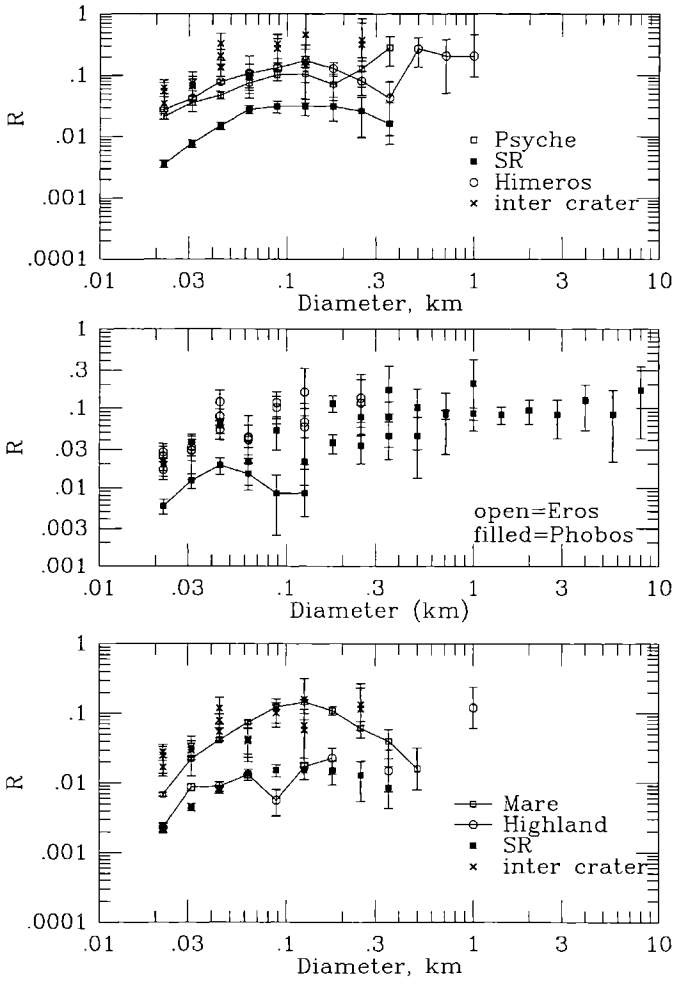

FIG. 3. (*left*) (a) R-plot (Crater Analysis Techniques Working Group, 1979) of crater densities within the three largest craters on Eros and intercrater terrain. Data for Psyche, Shoemaker Regio (surface of Shoemaker crater, Sh), and Himeros are at 3–5 m/pixel. The intercrater terrain data are at 2–3 m/pixel in areas at 5° S, 205° W and 10° S, 242° W, with 1 m data at 3° S, 28° W. (b) Eros and Phobos crater densities. Phobos data are from Viking images for the global crater data above 1 km diameter, and for selected areas at sizes down to 200 m diameters. The two sets of Phobos data at <200 m diameter are from Mars Orbiter camera data at ~4 m/pixel; one area is in rolling terrain east of crater Stickney, the lower, connected set is from the western wall of Stickney (data are from Thomas *et al.*, 2000). The high-resolution Eros and Phobos data in hilly intercrater areas are indistinguishable; both show some fall off relative to saturation below 100 m size. All data were collected by P. T. (c) Comparison of Eros and the Moon. Eros data are from Shoemaker Regio and the intercrater terrain data also shown in Fig. 3a,b. Eros data collected by P. C. T., lunar data by M. S. R. Lunar data are effectively 7 m/pixel (see Fig. 5 for lunar areas). Both sets of data show fall off in relative density below 100–200 m diameters, and both Eros and lunar data show the difficulty of age comparisons if crater erasure mechanisms are different in various terrains.

STRUCTURAL ELEMENTS

Structural features are abundant on Eros (Veverka *et al.*, 2000; Prockter *et al.*, 2002; Thomas *et al.*, 2002b) and include chains of pits, sinuous and linear grooves, ridges and scarps, and rectilinear craters (Fig. 4). Lineation sets on Eros suggest a global fabric that was most likely caused by impact events (Veverka *et al.*, 2000; Prockter *et al.*, 2002; Thomas *et al.*, 2002b). The large variation in directions, patterns, and relative ages of the lineations indicate that they were undoubtedly

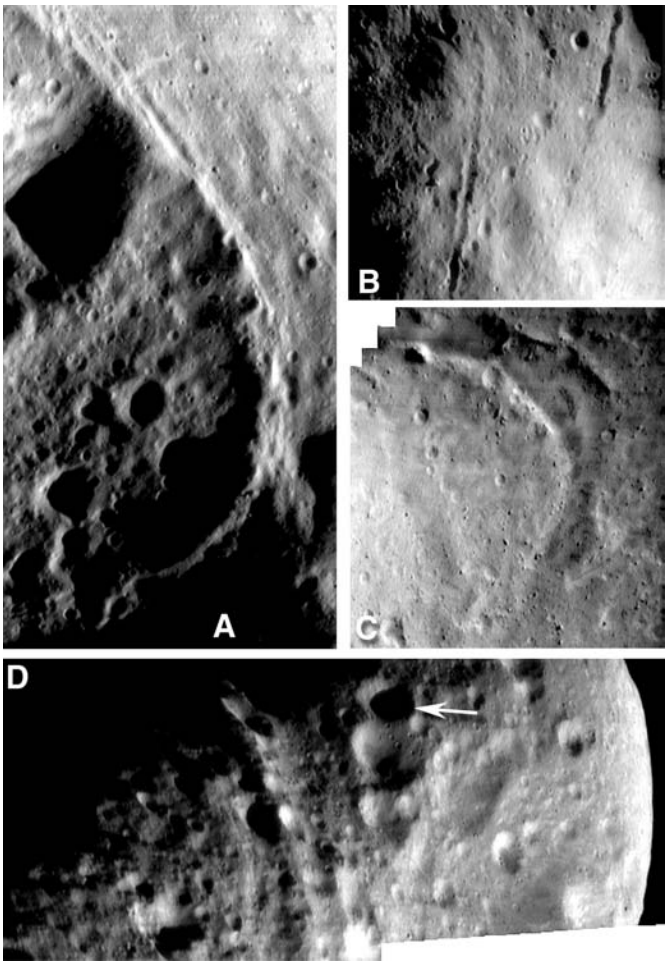

FIG. 4. Structural elements. (a) Central segment of Rahe Dorsum; note the orthogonal shape of the 2.6 km diameter Tutanekai crater at upper left (56.5° N, 2.6° W) indicating structural control (METs = 131893649–131893825). (b) Pitted grooves with levees (frame width ~1.1 km; METs = 135343994–135345734). (c) Termination of Rahe Dorsum inside Himeros crater; here the scarp transitions to a graben (see Fig. 1b label "RD" for context; METs = 0134011958–0134012810; width of mosaic ~1.8 km). (d) Large set of parallel ridges/graben known as Calisto Fossae (METs = 131177449, 131177643, crater indicated with arrow is ~810 m diameter at 17.0° S, 170.2° W).

formed during many different unrelated events (Veverka *et al.*, 2000; Prockter *et al.*, 2002; Thomas *et al.*, 2002b). A subset of the grooves has pitted segments, similar to grooves found on the martian moon Phobos. These Phobos examples are interpreted to indicate fractures that have opened to sufficient widths and depths to allow some drainage of loose material into voids (Horstman and Melosh, 1989).

Rahe Dorsum is a prominent ridge system that spans the northern hemisphere (18 km length) and geometrically defines a planar slice through the asteroid (Thomas *et al.*, 2002b; Prockter *et al.*, 2002). This ridge cross-cuts structures such as Himeros, indicating that it was created after Eros reached its current shape (Veverka *et al.*, 2000; Prockter *et al.*, 2002). It is continuous across more than a third of an Eros circumference, and its morphology is consistent with a compressive fault plane through consolidated or coherent material. A set of parallel ridges (Calisto Fossae) on the opposite side of Eros is coplanar with Rahe Dorsum and almost certainly represents the continuation of this same fault, or plane of weakness. The morphology at Calisto Fossae contrasts with that at Rahe Dorsum in that it is more consistent with an extensional environment (Thomas *et al.*, 2002b). The shape of Eros may also reflect this planar feature in the form of a smooth planar facet west of Shoemaker crater (Thomas *et al.*, 2002b). The different expressions of this planar fabric probably reflect different stresses applied at different times. The stresses that exploited the structural elements most likely were imposed by impacts, though the modeling that assign a particular source crater has not been done for Eros, as it was for structures and craters on Ida (Asphaug *et al.*, 1996).

The presence of a global fabric indicates Eros has not been disaggregated and reassembled. The multitude of fractures evidenced by the grooves and ridges indicate the object has, however, been thoroughly fractured. The measured density and estimated porosity of Eros also suggest pervasive fracturing of much of the object (Wilkison *et al.*, 2002) through repeated large-scale impacts over the lifetime of the body. Terrestrial studies indicate that for Meteor Crater (Arizona) the bedrock beneath the crater is heavily fractured to a depth of 180 m, close to the depth of the crater itself (190 m; Ackermann *et al.*, 1975). By analogy the regions of Eros beneath Psyche and Himeros must be heavily fractured to within a few kilometers of the center of the asteroid. Morphological features such as continuous grooves, steep continuous ridges, and fault planes suggest, despite the heavy fracturing, that the asteroid possesses mechanical strength to some degree and is not strictly a gravitationally bound granular object (Thomas *et al.*, 2002b; Prockter *et al.*, 2002; Wilkison *et al.*, 2002).

IMPACT CRATERS

Crater Densities

Impact crater densities can be used to investigate relative ages of surface units, production populations, possible approach to saturation, and degradational processes. The NEAR images provided the first reliable observations of sub-100 m craters on an asteroid. Veverka *et al.* (2001a) and Chapman *et al.* (2002) found that much of the surface approached "empirical saturation", but at sizes below about 100–200 m the crater density was progressively lower than predicted for nearly saturated surfaces and did not have a slope expected of production populations. We have made additional crater density measurements to attempt to determine the relative ages of large features on Eros and to examine the relative crater densities at small sizes compared to the martian satellite Phobos and the Earth's Moon, for which comparable resolution data exist.

Our crater density data are generally consistent with those independently derived by Berthoud *et al.* (2001). Himeros and Psyche have similar crater densities, and these are well distinguished from the lower densities inside Shoemaker crater. Crater counts have been obtained from images with 3–5 m/pixel scales, and should be reliable to ~30 m diameters (see caveat below). For comparison we have measured the crater density at slightly higher resolutions in three areas outside large craters. These data (Fig. 3) have slightly higher densities at all diameters than do the large crater interiors, but also show a relative decrease at sizes below 100 m diameter.

To test if the characteristics of crater densities on Eros are unique to that body, or whether conditions found elsewhere can produce features such as the decrease of slope on the R-plot at diameters below ~100 m, comparison was made to Phobos. The Phobos data (from Thomas, 1998; Thomas *et al.*, 2000) include a global data set (>700 m diameter), and some local data at good viewing down to pixel scales of ~4 m. The Phobos and Eros crater densities between 30 and 200 m are similar except for the steep topography (slopes ~20°) within Stickney crater, which has a substantially lower crater density. The similarity of the maximum crater densities on the two objects, and the presence on both objects of decreasing relative densities between crater sizes of ~150 to 30 m, suggests that the decrease in relative density in this size range is due to a mechanism that is not unique to Eros. Furthermore, on both objects the decrease is observed for areas having different crater densities, that is, these are not saturation curves, nor are they consistent with usual expectations of production populations (Chapman *et al.*, 2002). Additionally, we note that from moderate resolution Galileo images of Gaspra (~60 m/pixel) Carr *et al.* (1994) postulated a drop off in crater densities below 200 m and attributed this to preferential degradation of smaller craters formed in a thick regolith (>20 m).

To better understand the small crater densities we examined a region on the Moon imaged at high resolution (~7 m/pixel) by *Lunar Orbiter III* where the mare and highlands should have received the same cratering history (both primary and secondary). The lunar orbiter image was chosen because it has similar spatial resolutions and lighting geometry as the MSI global images (Fig. 5). Here the lunar mare has substantially greater crater densities than the older highlands (Fig. 3), and both areas show a fall-off from an equilibrium slope at sizes less than ~100 m (see also Trask and Rowan, 1967). The highland data in this example happen to approximate closely the Shoemaker Regio data (we note the data were collected by different authors; P. C. T. = Eros, M. S. R. = Moon). The density of small craters on the mare can vary considerably, and in some places, as measured by other workers (Moore, 1964; Shoemaker, 1965; Trask and Rowan, 1967; Soderblom, 1970), can show some fall off at sizes <200 m (not attributable to resolution effects).

We speculate that the explanation of the decreased R-plot slope at small diameters on Eros and Phobos is primarily due

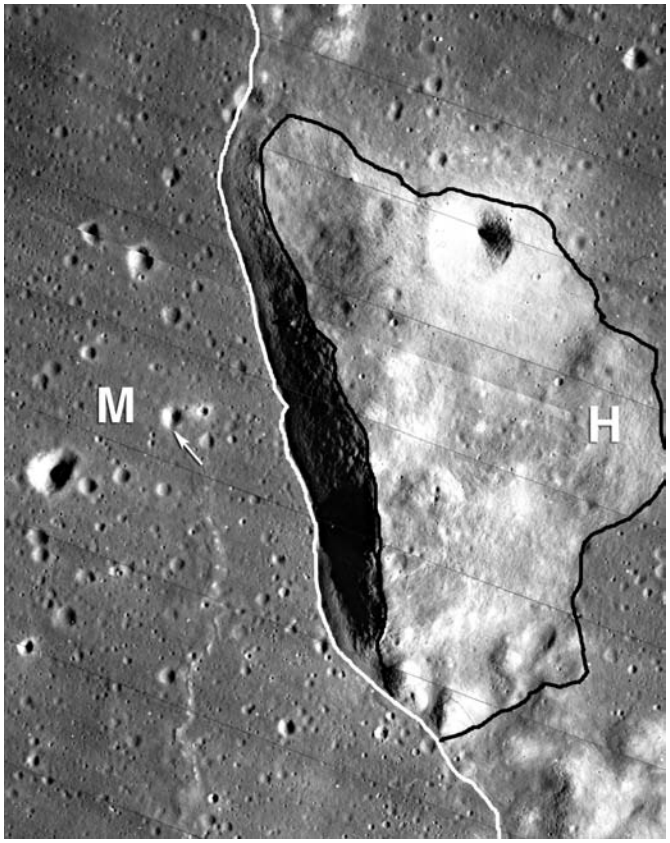

FIG. 5. Lunar Orbiter frame (LO3 200M) used in crater counting. Mare area delineated with white line and labeled "M", highland area marked with "H" and black outline (small crater marked with arrow centered at 2.8° S, 317.5° E, frame width ~10.6 km, 6.7 m/pixel, incidence angle ~71°).

to the destruction of small craters by processes in addition to those predicted whereby new craters remove some fraction of preexisting craters. Mutual obliteration by craters is the process apparently responsible for producing "saturation" slopes (–2 on cumulative plots, –3 on differential plots, horizontal on standard R-plots). Veverka *et al.* (2001a) proposed the idea that seismic shaking of a loose regolith on Eros causes preferential erasure of these smaller craters on Eros. Seismic effects (Greenberg *et al.*, 1996) might be able to efficiently result in crater erasure, although the specific model presented by Greenberg *et al.* (1996) would not predict a substantive change in the slope of part of an R-plot. To form a crater distribution such as those in (Fig. 3) the effects of shaking need to be more effective on the smaller craters. Such a situation might derive from shallower material being looser than deeper material, such that for larger craters the efficacy of seismic jolting decreases not only due to crater size but also by smaller response to similar stresses imposed by seismic accelerations. Since the crater morphologies do not indicate sharp discontinuities in the regolith with depth, stronger material may have to gradually grade into the upper, less consolidated, materials.

The lunar data support a key role for material strength properties in determining observed crater densities. Because the younger mare surface supports a higher density of craters than the highlands, the latter area must undergo rapid degradation and erasure of small craters (Trask and Rowan, 1967). This enhanced removal is most likely due to thicker regolith and steeper slopes in the highlands relative to the younger, nearly horizontal, mare deposits. We note that the highland unit here (Fig. 5) comprises a portion of the Flamsteed ring (crater rim) and may thus represent unusually steep and fractured highland topography, thus representing an extreme case of small crater erasure. Similar crater count data for several average highland areas are presented in Wilcox *et al.* (2002) showing that highlands are depleted (relative to mare areas) in craters over the size range 50–200 m by a factor of 1.5 (from images with incidence range of 65–80° and resolution range of ~1 m/pixel). *Apollo 16* landed in a heavily degraded 75 m diameter crater (in the lunar highlands) and the astronauts reported that the "landing area is saturated with these old craters so that the few young sharp-rimmed craters provide a notable contrast to the pervasiveness of the old craters" (Young *et al.*, 1972). The lunar example suggests that asteroids with a substantial regolith will have a depletion of craters at sizes smaller than 100–200 m.

Most terrain on Eros is not horizontal; average slopes relative to gravity are ~8° to 10° (Zuber *et al.*, 2000; Thomas *et al.*, 2002a), and 18% of the surface slopes are >15°, a condition favoring gravity driven slides, slumps, or creep. Note that much of the inter-crater area on Eros has slopes in the range of 5–10° (see Figs. 2 and 3 of Thomas *et al.*, 2002). Evidence of downslope motion of material is common on Eros (Veverka *et al.*, 2001a; Thomas *et al.*, 2002a), and may contribute to erasure of craters at a rate greater than expected on horizontal areas similar to that of the lunar highlands.

An observational effect on measured crater densities may also arise from topography for the smaller craters (relative to pixel size). Most crater density measurements on the Moon, Mars, Mercury and large icy satellites cover regionally horizontal (slopes <1°) surfaces. The complex topography on Eros can make identification of a small crater more difficult than would be the case for an identical crater morphology and incidence angle on a horizontal surface. Emission angle also affects how well craters can be identified, especially if the rims are not sharp. On Eros and other irregular objects craters are nearly always observed at non-zero emission angles, frequently at over 20°, and this condition may further increase the difficulty of seeing smaller craters. We have assumed that our crater counts are good to sizes that are 8–10 pixels across. Discussions of effects of emission and incidence angle on feature identification can be found in Howard and Larsen (1972), Lissauer *et al.* (1988), and Collins (2000). We can confidently report that the drop off in crater densities on Eros is real and not an artifact of viewing for sizes down to 50 m globally (and smaller sizes locally from the highest resolution data). The drastic differences between mare and highland crater densities show that the observational effects are secondary; physical effects of crater obliteration at sizes below 200 are the primary cause.

Chapman *et al.* (2002) favored the idea that the relative decrease in crater density below 200 m diameter may be due to an impactor population deficiency at small sizes (Bell, 2001). If so, this must also apply to the martian satellites which have a similar paucity of smaller impact craters. Since the impactor population most likely differs from the asteroid belt to Mars, the fact that the Phobos data indicate a similar population of smaller craters may be inconsistent with the small impactor deficiency hypothesis. Whatever the role of impactor population, the Phobos and lunar highland data indicate that the similarity of the shapes of relative crater density curves may derive at least in part from common factors such as slopes and the presence of regolith (mega-regolith) contributing to enhanced crater erasure at sizes below ~200 m.

Crater Morphology

Craters on Eros exhibit a range of morphology from those that can be described as distinct (or crisp) with raised rims and bowl-shaped interiors (see also discussion in Chapman *et al.*, 2002), to those that are extremely rounded and nearly rimless with infilled interiors (Fig. 6). All craters exhibit smooth interiors with no evidence of terracing or concentric mounds that are seen in many lunar craters (Fig. 7). On the Moon, interior terracing of 100 m scale mare craters has been proposed to indicate excavation through a loose unconsolidated regolith to a coherent substrate (Oberbeck and Quaide, 1967, 1968; Quaide and Oberbeck, 1968). This morphology is rarer in lunar highland craters, indicating a thicker or more gradational regolith or a lack of a coherent substrate. We have found no clear examples of interior terracing or central mounds in any Eros craters. A handful of craters has been identified that may show signs of discontinuities in their walls; three examples are shown in Fig. 8. If indeed these three craters do indicate a strength discontinuity, in all cases this layer or interface lies tens of meters below the surface. Degraded craters (smooth rim, infilled interior) on Eros, especially at sizes above 100 m (Fig. 6), are the norm and are responsible for Eros' undulating and steeply sloping surface (average slope 8° to 10°) and compose the intercrater hilly terrain (rough areas between the larger, >1 km, well-preserved craters).

The depth/diameter ratio of bowl-shaped simple craters (Fig. 9) is a product of the crater excavation, collapse, and post-cratering modification. Distinct (or crisp) craters on Phobos approach the lunar value of 0.2 (Thomas, 1979). Data on the crater diameters and length of shadows in Eros crater interiors were collected using the program "POINTS" developed by Jonathan Joseph (see Thomas *et al.*, 2002a). Incidence angles were high enough, generally >65° and <80°, to give shadow lengths within a quarter diameter of the crater

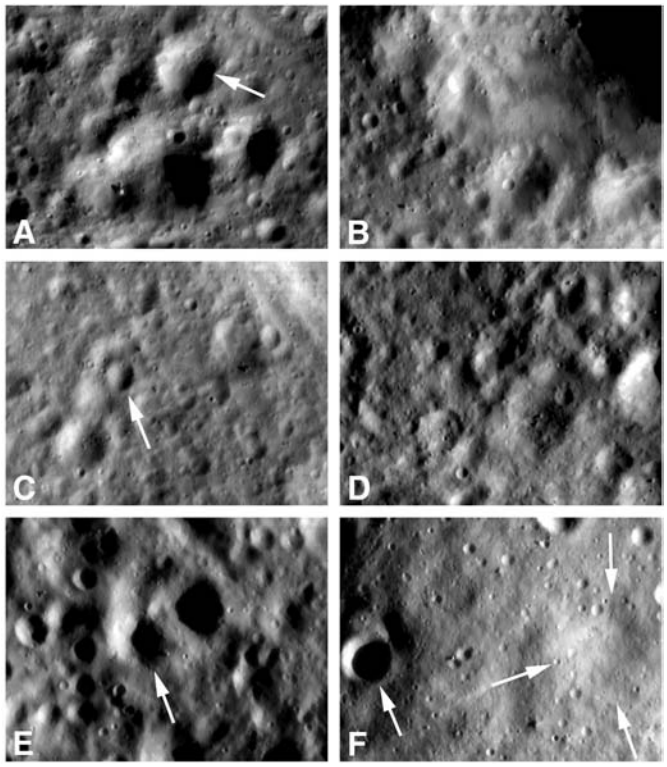

FIG. 6. Typical intercrater regions of Eros. Crater forms range from heavily degraded to sharp (crisp), with the former type dominating. (a) 450 m diameter crater indicated with arrow is centered at 50.5° N, 269.8° W; MET = 132576924, frame width ~2200 m, incidence angle ~72° (note that incidence angle can range over 30° within a frame due to Eros' extreme excursions from sphericity). (b) Large crater (Jahan) that dominates the upper right quadrant of the frame is ~1800 m in diameter centered at 75.8° N, 290.8° W; MET = 132588624, frame width ~2200 m, incidence angle ~62°. (c) Relatively sharp (crisp) rimmed crater (arrow) is ~200 m diameter centered at 59.8° N, 55.2° W; MET = 132907812, frame width ~2230 m, incidence angle ~64°. (d) Center of frame ~49° N, 49° W; MET = 135613839, frame width ~2190 m, incidence angle ~70°. (e) Relatively degraded crater (arrow) is ~360 m diameter; image is centered at 48.7° S, 180.6° W; MET = 139468893, frame width 1580 m, incidence angle ~78°. (f) Sharp (crisp) rimmed crater indicated with left arrow ~360 m in diameter, centered at 71.9° S, 353.4° W, note the heavily degraded crater that is nearly erased (right arrows circle rim); MET = 140581300; frame width 2160 m, incidence angle ~69°.

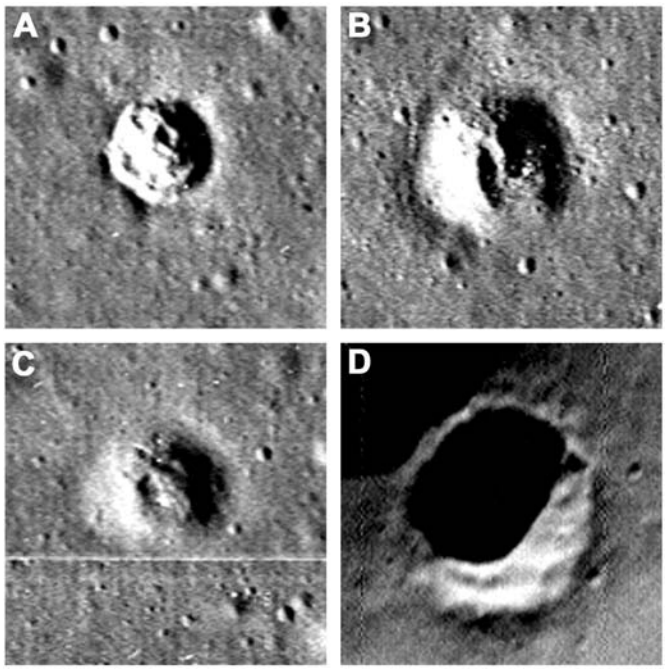

FIG. 7. Different degradation states of concentric mound craters on the Moon; arranged (a) to (c) (younger to older, respectively). The concentric hummocky morphology has been interpreted to indicate the presence of a sharp strength discontinuity between a loose unconsolidated regolith and a coherent substrate, see text for details (Lunar Orbiter image LO3 195 H, 80 cm/pixel, incidence angle 71°, (a–c) are each 128 m across). (d) Craters possibly similar to the lunar examples have been found on the martian moon Phobos (MOC Image 55103, crater diameter ~150 m, ~1.5 m/pixel) indicating locally thinned regolith (Thomas *et al.*, 2000).

center. The depths from the crater rim to these points on the crater floors were then scaled to a nominal parabolic crater shape and the maximum crater depth calculated. The shapes of the craters and the variety of viewing conditions guard against effects of single incidence angle artifacts noted by Chappelow and Sharpton (2002). Re-measuring craters from multiple images with varying incidence and emission angles tested the validity of our technique. The results indicate the technique is reliable to a few percent of the diameter for circular craters, that is, a crater may have a d/D of 0.13 ± 0.03, the uncertainty here being solely the standard deviation of several measurements. Uncertainties in our plots have been estimated assuming an error of 2° in the incidence angle and 1 pixel errors in measurement of crater diameters and shadow lengths, and contribution of apparent solar diameter. Error bars in the plots (Fig. 9) are the root sum errors from the different sources. Depths of some of the larger craters may be more uncertain because of the generally rougher rim topography and effects of curvature of the whole object.

A linear fit to all the d/D measurements gives a slope of 0.13. The three largest craters, Himeros, Shoemaker, and Psyche, were measured from the digital shape model, and require taking the shape of Eros into account (Thomas *et al.*, 2002a). Psyche has a near-lunar fresh crater depth/diameter, while Himeros and Shoemaker are shallower (~0.12 for both). Smaller size ranges, from 0 to 200 m and from 0 to 2500 m diameter are also shown (Fig. 9), with lines showing the appropriate linear fits to the data for those size ranges: a slope of 0.14 for 0–200 m, and a slope of 0.12 for 0–2500 m. The maximum depths of craters, perhaps representing the conditions of a fresher population, would be fit with a higher slope; for the 0–500 m craters this would approach values of 0.19–0.2, a quantity indistinguishable from that of fresh lunar craters (Pike,

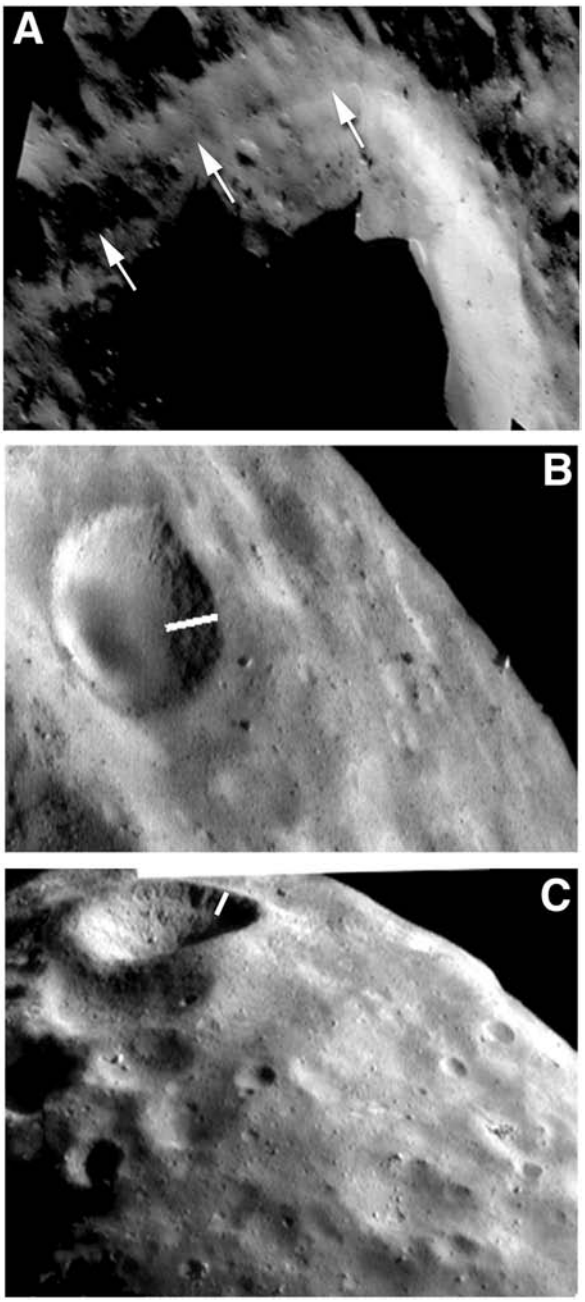

FIG. 8. Only examples of crater walls on Eros that show hints of layering that may indicate a mechanical strength interface. (a) Portion of MSI low Sun angle (~70°) mosaic of Gamba crater, distance along slope from the rim to indicated lineation (arrows) is ~100. This lineation appears to cut through the crater at an angle intersecting the rim at one point. Correcting for viewing geometry and topography this section of the lineation is about 40–50 m down-section below the rim (~1050 width of image, METs = 147954658–147955672). (b) Crater diameter ~300 m (8° S, 169° W), 55 m along slope (white line) to lineation, true down-section depth is >25 m (MET = 155807976). (c) Crater diameter ~650 m (5.4° S, 175.9° W), 90 m along slope (white line) to lineation, true down-section depth is >50 m (MET = 134783314). None of these examples clearly define a mechanical strength interface; the main point is that no examples similar to those found on the Moon and Phobos have been found on Eros.

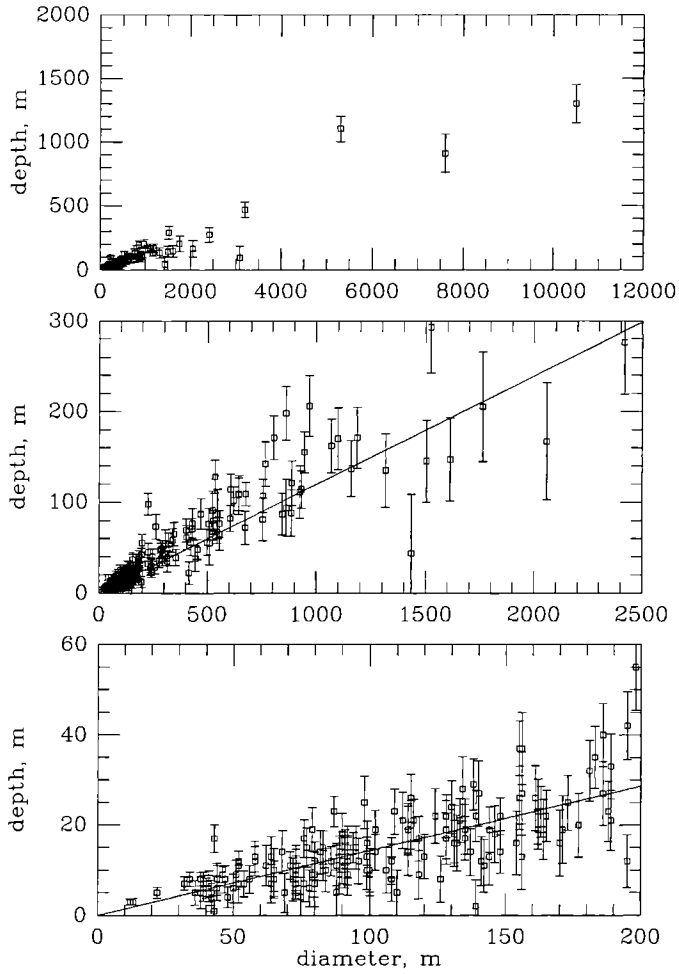

FIG. 9. Crater depth to diameter ratios on Eros. Depths were obtained by shadow measurements with correction for fractional width of crater covered by shadow; see text for details on measurement and uncertainty estimates. Depths of the three largest craters are from the shape model, relative to local gravity equipotential surfaces. Solid lines in lower two panels are linear fits to data within the size range plotted; a slope of 0.14 for 0–200 m; a slope of 0.12 for 0–2500 m.

1977). Very fresh craters on the Moon reach a *d/D* of ~0.2 (Pike, 1977); those on asteroids Gaspra and Ida average slightly shallower, ~0.14 to ~0.15, respectively (Carr *et al.*, 1994; Sullivan *et al.*, 1996).

Sullivan *et al.* (1996) discussed in detail potential explanations for the lower *d/D* values for Ida and Gaspra relative to Phobos and the Moon, including possible systematic errors introduced by their photoclinometric measurements, relatively poor spatial resolution, and off nadir viewing. They concluded that the *d/D* measurements were good to 10% and thus gave clues to geologic processes on the asteroids. They favored relatively rapid burial and degradation by widely dispersed ejecta across the asteroid over time. However, they noted that this explanation failed to explain the lunar-like *d/D* for Phobos craters.

We speculate that the enhanced destruction of craters on slopes and deep regolith results from effects of seismic shaking of the asteroid. Although seismic shaking has previously been modeled (Cintala *et al.*, 1978, 1979; Asphaug and Melosh, 1993; Greenberg *et al.*, 1996) as a general process specific calculations for Eros remain to be made. Further investigation of seismic transmission and response of a regolith with a gradation of porosity may yield predictions of high efficiency of erasure for sub-100 m crater. The maximum *d/D* values suggest there is little net difference in the excavation and collapse of these craters formed in a gravity environment less than 1/100th that on the Moon. Rims are visible on many of the Eros craters (Figs. 2 and 6; see also Fig. 2 of Thomas *et al.*, 2002a), and indeed mark the boundaries of Psyche and Shoemaker craters. While the ejecta component of these rims may be smaller than on the Moon, any minor rim differences between Eros and the Moon do not affect the *d/D* values at a detectable level.

Block Production by Impact Cratering

Previous work has suggested that the impact event that formed Shoemaker crater produced a large population of blocks (or boulders) that littered much of Eros' equatorial region (Thomas *et al.*, 2001). Indeed, over 40% of the volume of large blocks on Eros are contained within Shoemaker crater. In our mapping we have been unable to make links between any other large craters (>500 m diameter) and particular block populations. In fact the only other crater on the asteroid that we have observed to have a genetic relation to a block population is the crater in which *NEAR Shoemaker* landed (Fig. 3 of Veverka *et al.*, 2001b), which was observed at resolution of ~2 to 5 cm/pixel. Thus, either impact events on Eros do not typically produce significant numbers of boulders at scales >5 m, or boulders on Eros are for some reason short-lived. The latter possibility seems unlikely as Shoemaker crater is most likely not a young feature in absolute terms (though it is younger than Psyche and Himeros craters), suggested by the number of superposed craters (see "Crater Densities" section). Micrometeorite impact decay of coherent rocks is a slow process (1 mm/Ma; Crozaz *et al.*, 1971; Arvidson *et al.*, 1975) discounting *in situ* disintegration of boulders. Though direct impact by a macrometeorite will result in catastrophic fragmentation of boulders, the fact that so many boulders exist on Eros and that superposed craters show Shoemaker crater is ancient, such a process is clearly not efficient on Eros.

On the Moon craters with abundant block (either interior and/or exterior to the host crater) populations (blocks >1 m diameter) are generally not common in the existing submeter resolution Lunar Orbiter frames. On mare units, such craters compose ~1% of all craters; however, these blocky craters plus their ejecta cover ~12% of studied areas, thus giving the appearance that the blocky craters make up a larger percentage of the population of all craters (Wilcox *et al.*, 2002). Craters with abundant blocks are even rarer in the lunar highlands, possibly signaling an incoherent or more fractured substrate (see discussion below). Thus, from the lunar example it should not be surprising that it is difficult to find craters with abundant blocks on Eros (at the scales seen in 5 m/pixel images), especially since the lunar highland regolith (rather than the lunar mare regolith) is a better analog for the regolith of Eros in terms of depth and mechanical properties (see below).

REGOLITH

Surveyor lander images of the lunar mare confirmed that the lunar surface is highly fragmented and poorly sorted, leading to the first use of the term *regolith* in an extraterrestrial sense—"a layer of fragmental debris of relatively low cohesion which overlies a more coherent substratum" (Shoemaker *et al.*, 1968; Shoemaker and Morris, 1968). These early discussions of the regolith excluded large-scale crater ejecta from the definition, specifically stating, "We do not intend to apply the term regolith to such widespread blankets of fragmental ejecta associated with large individual craters on the Moon" (Shoemaker *et al.*, 1968). Strictly speaking these early definitions considered only material produced over long periods of time by micrometeorite bombardment of *in situ* local materials. High-resolution *Lunar Orbiter* images (~1 m/pixel) revealed abundant evidence of a global lunar regolith in the form of boulders, partially buried or infilled craters, and slumps and slides on crater walls and on massif slopes. Apollo astronauts sampled the regolith to several meters depth, probed it with active and passive seismic experiments, and photographed it at extremely high resolution (see summaries and references in Heiken *et al.*, 1991 and Wilhelms, 1987). Conceptualizing the depth of the regolith on the lunar mare is perhaps a simpler exercise than in the lunar highlands or on Eros. As pointed out in a study of highland regolith by Cintala and McBride (1995):

> The concept of "regolith thickness" begins to lose its meaning in the lunar highlands, which are so pulverized from accumulated impacts that they have no bedrock layer for reference. When the chaotic deposits from a large crater are included, as in this case, the local definition of the regolith becomes more philosophical in nature.

In much of the lunar highlands, and probably on Eros, it is unlikely that there is a clear-cut interface between a loose fragmental layer and a continuous coherent substrate as in the lunar mare, but rather a continuum from heavily fractured to less fractured materials. Interpretations of surface structural features identified in MSI images and comparisons of the density and porosity of ordinary chondrites with the density of Eros led to the conclusion that in the case of Eros fractures may reach well into the interior of the body (Wilkison *et al.*, 2002). Here we use the term regolith to refer to the loose

unconsolidated material that comprises the upper portions of the asteroid whether or not it formed *in situ* or was emplaced as ejecta from an impact event somewhere on the asteroid.

As in the case of the *Lunar Orbiter* observations of the Moon, NEAR-MSI images provide abundant evidence of a loose and highly mobile fragmental layer of debris, or regolith, in the form of debris aprons, partially buried boulders, infilled and subdued craters, streamers, slumps, and talus cones (Figs. 10–13). Evidence of a regolith in one form or another can be found in nearly every high-resolution (better than 5 m/pixel) image of Eros (see also Veverka *et al.*, 2001a; Thomas *et al.*, 2002a).

A key question regarding Eros' regolith is its global distribution and thickness; is it everywhere thick (tens of meters) or does it thin locally to meter or submeter depth? Is bedrock exposed anywhere at the surface? Since impacts at all scales contribute to regolith formation, a first-order estimate of the average global regolith thickness can be obtained by summing

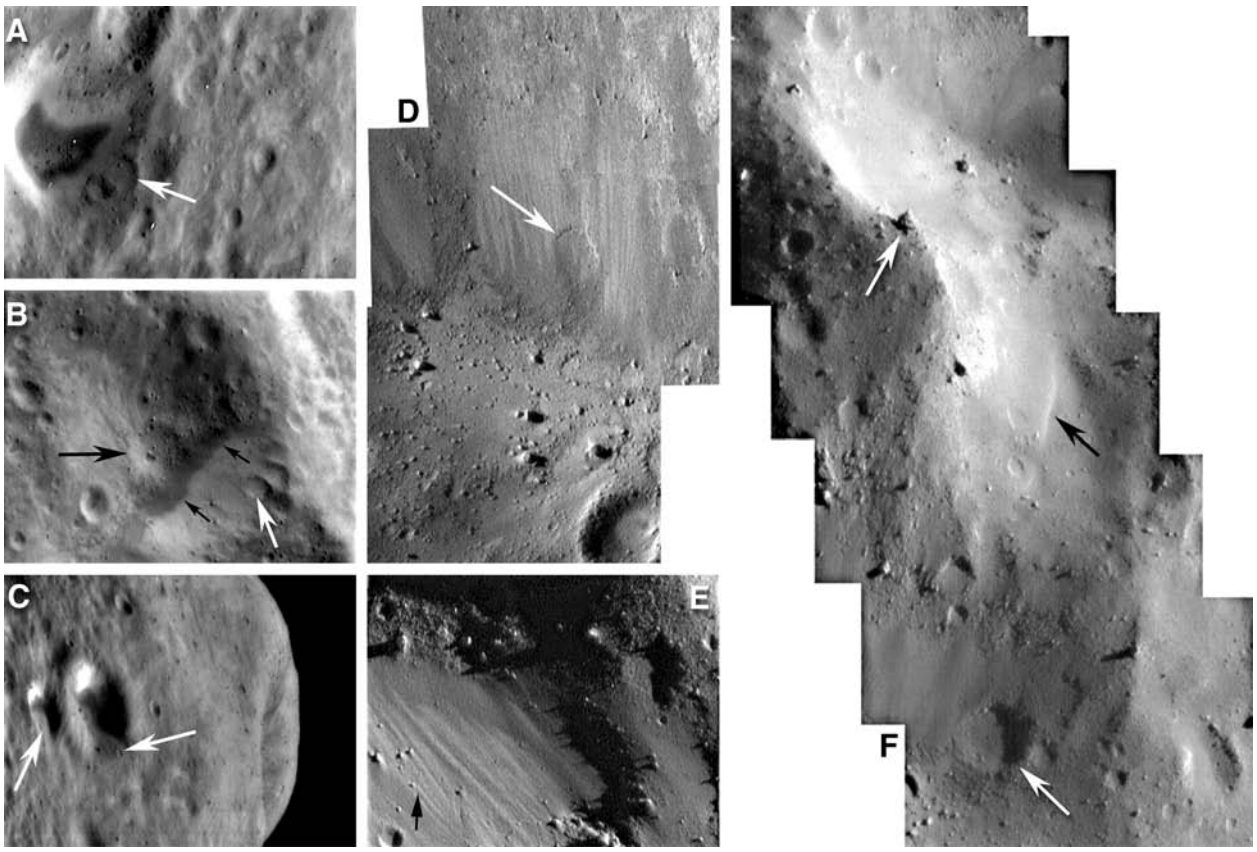

FIG. 10. Indicators of a loose fragmental regolith are common on Eros, and can be found in nearly every high-resolution image (better than 5 m/pixel). (a) Arrow indicates ~170 m crater on rim of Avtandil (see Table 2) that is partially buried by regolith moving downslope. If the crater had an initial *d/D* of ~0.2 and it is ~50% filled, the regolith is here 10–20 m thick. Note the higher reflectance deposits completely lining the steep interior walls of Avtandil and the lower reflectance floor deposits. Both reflectance features are interpreted to result from grain segregation during downslope movement of regolith (MET = 139020130, width of frame ~1520 m). (b) View centered on Aida crater (9° N, 131° W) located on the southwest rim of Psyche crater. White arrow indicates ~180 m diameter crater that is mostly buried by a debris apron on the steep inner rim; the amount of burial is consistent with 10–20 m depth of fill. Small black arrows show downslope direction on debris apron; the tips of the small black arrows also indicate a sharp transition to a lower albedo deposit (MET = 133262465, width of frame ~2170 m). Large black arrow highlights extremely degraded and infilled ~410 m crater on Aida floor. (c) Eros' southern hemisphere, Dulcinea crater (right arrow, 75.4° S, 285° W, 1.6 km diameter) and unnamed crater (left arrow) both exhibit higher albedo wall deposits, and inflow of material from outside of crater (tip of arrows, especially left arrow) (MET = 144717576, left side of frame to limb ~4 km). Because slopes are relatively low in this area, the flows into these craters are most likely surface flows of impact ejecta. (d) Interior view of Leylie crater highlighting debris apron on steep wall (top) and embaying floor (bottom) (3.0° S, 23.5° W, 1.9 km diameter). Partially buried crater (arrow) is ~80 m in diameter, the amount of filling is consistent with 5–10 m depth of debris apron (METs centered on 155988400; width of each frame ~400 m). (e) Relatively fine-grained debris apron on opposite side of Leylie crater from that shown in (d). Note the downslope (to upper left) striations that in some cases appear to be the result of gouging by boulders sliding downhill (small black arrow). Crater at lower left edge of frame is 30 m in diameter (MET = 1558837414, width of frame ~400 m, for regional context of both (d) and (e) see MET 135326689). (f) Unnamed doublet crater (6.5° S, 170.8° W) resurfaced with smooth deposits (black arrow). Boulder perched on septum (upper white arrow) of two craters is ~50 m diameter. Note also sediment apron (at bottom) on steep wall of third crater with partially buried 115 m diameter crater (lower white arrow) indicating depth of fill ~10 m (METs = 156076255–156076423, width of each frame ~570 m).

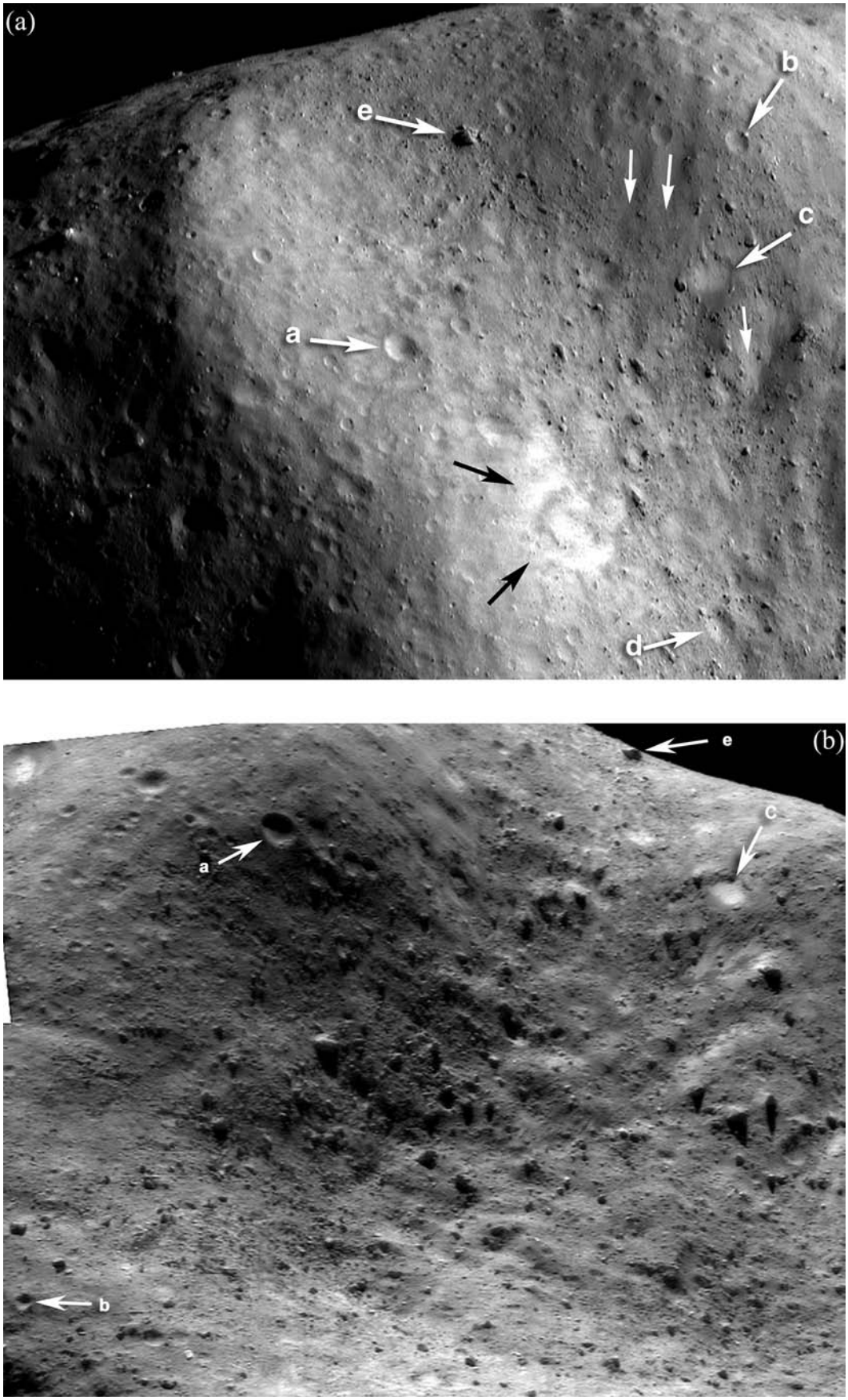
(a)
b
e
c
a
d
(b)
e
c
a
b

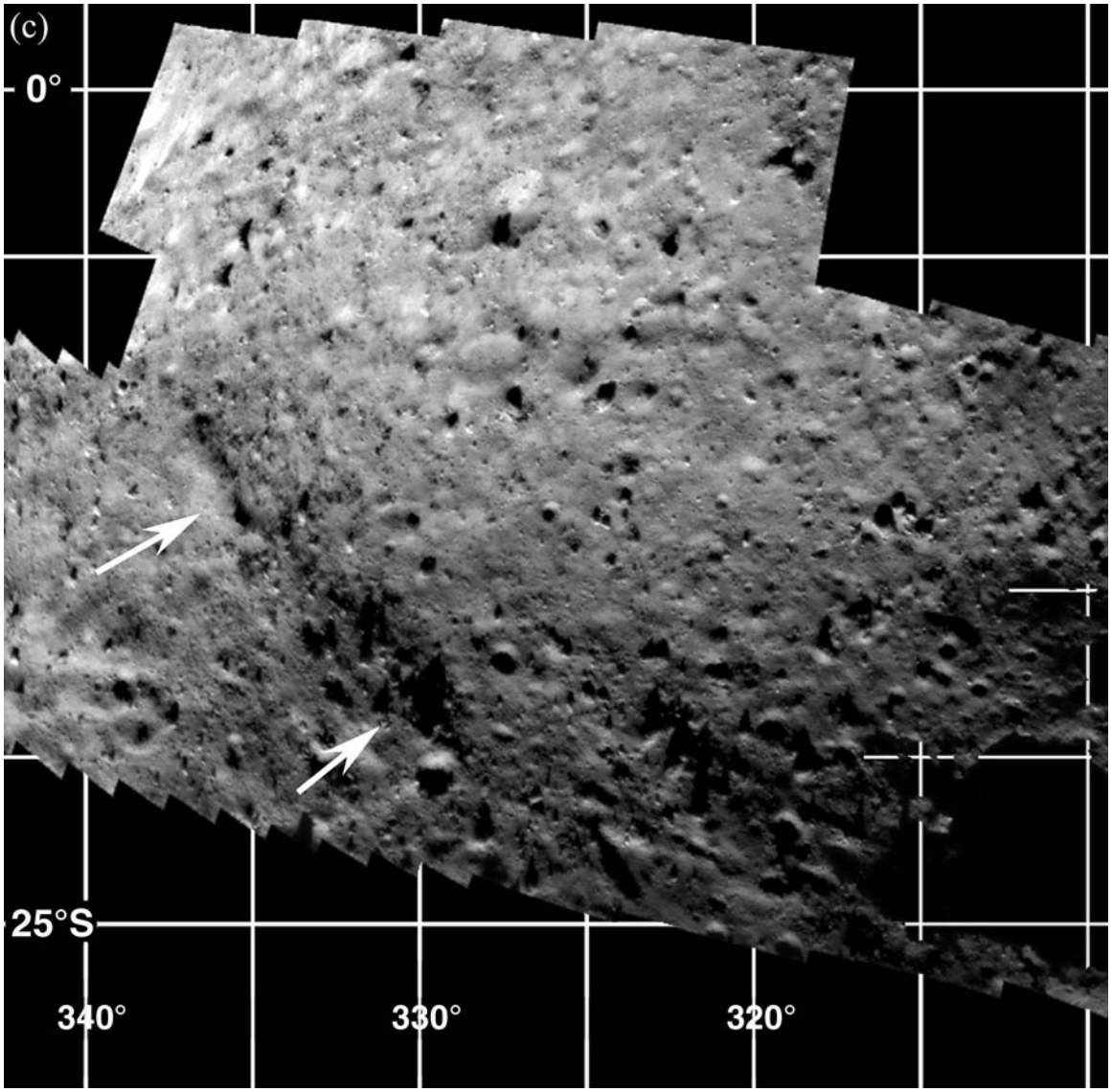

FIG. 11. *Facing page and above.* Shoemaker Regio is a rough, hummocky, boulder strewn layer of debris that covers much of the interior of Shoemaker crater (see Fig. 2 for context). (a) View of northwest portion of Shoemaker crater; small craters in all states of degradation are visible from pristine ("a" 190 m diameter and "b", 150 m diameter) to heavily degraded and infilled ("c" 280 m diameter and "d" 205 m diameter). Depths of burial of degraded craters "c" and "d" indicate the regolith here to be ~20 m or more in depth. The higher reflectance markings at the bottom of the mosaic correspond with some of the steepest slopes inside Shoemaker crater. Similar occurrences of like material occur elsewhere on the asteroid. Boulder marked with arrow "e" is ~120 m diameter (METs = 136402682–136403178). (b) Mosaic highlighting central portion of Shoemaker crater, note the high abundance of boulders and hummocks. The hummocks are consistent with large-scale slumping of interior materials indicating to tens of meters of loose material. Crater marked "c" and boulder indicated with arrow "e" are marked identically in (a). Sharp rimmed crater marked "a" is 210 m diameter centered at 13.7° S, 345.5° W, crater labeled "b" is found at 34.9° S, 350.8° W (METs = 136103971–136104033). (c) High-resolution mosaic showing steep west wall of Shoemaker crater (upper left) and rough hummocky floor (lower right). Prominent ridge indicated with arrows might indicate ghost structure of original rim (for context see Fig. 2) of Himeros crater or large accumulations of debris (METs = 156411946–156413266 and 156468946–156470159).

the excavated volume (about one half the volume of the crater cavities) of all craters and assuming a conservative retention rate of 25% to 50% (Asphaug and Melosh, 1993). This retention rate, not intuitively obvious because of the low gravity, has been supported observationally by comparison of estimates of Phobos' total ejecta volume and models of ejecta distribution across its surface (Thomas, 1998). For Eros we summed the excavated volume of all craters larger than 1 km in diameter (89 km^3) and divided this value by Eros' area (1125 km^2) to derive an average regolith depth of 20–40 m (retention of 25–50%) (Thomas *et al.*, 2001). On asteroids ejecta do not impact symmetrically, as they do on the Moon, due to the relatively

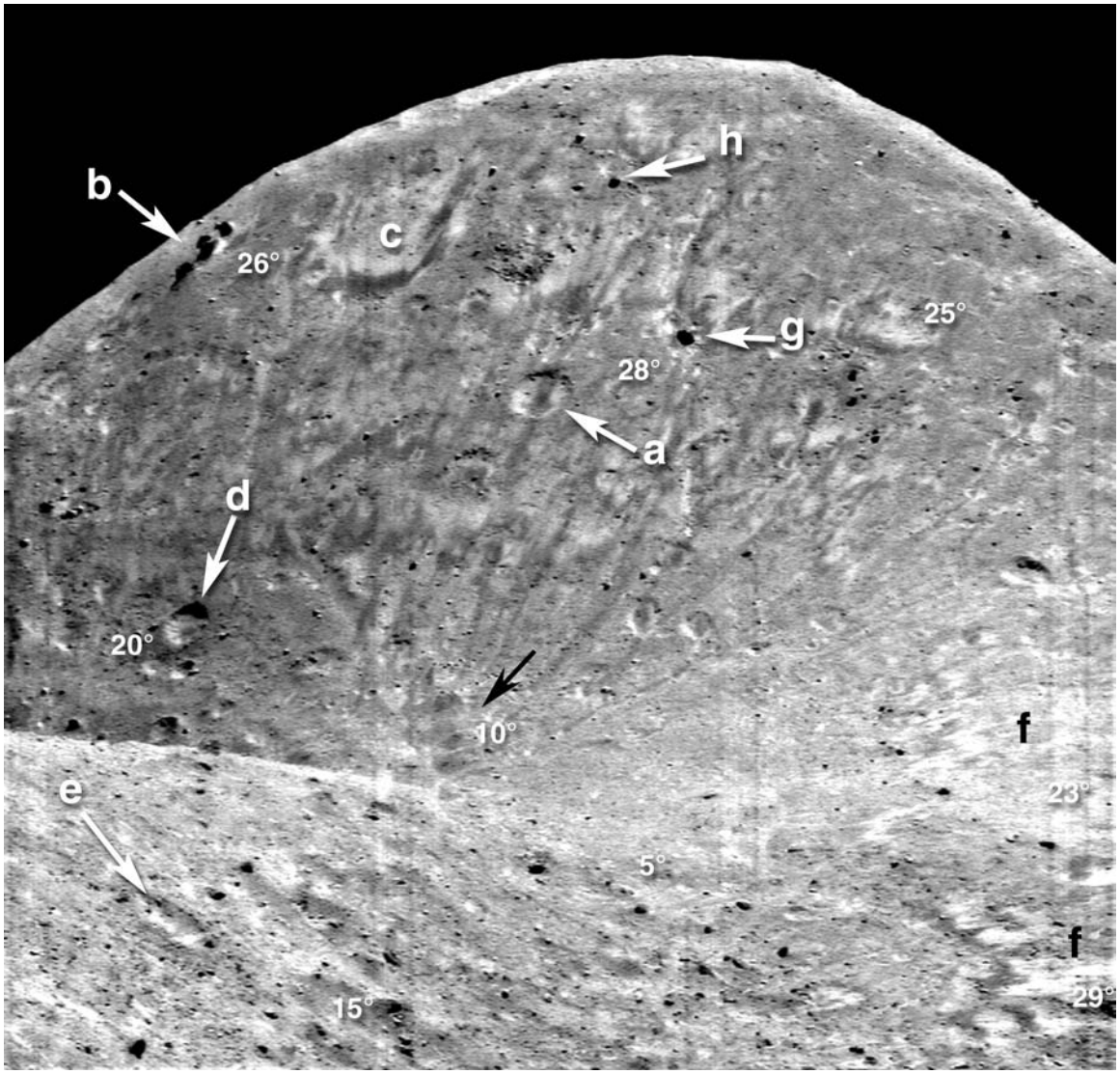

FIG. 12. Oblique view from southwest to northeast across Himeros crater centered on steep east wall (20–25° slopes). The interior of Himeros is distinguished by exposures of structural features and a variety of indications of downslope transport of regolith. Note the relatively low-albedo streamers that cross minor topographic obstacles (crater marked "a", 300 m diameter, 4.12° S, 264.3° W) unimpeded. The group of boulders (~75 m diameter) seen at "b" are each perched on a remnant pedestal of original substrate undermined by downslope movement of regolith. Circular feature at "c" is most likely a heavily degraded 1000 m crater. Crater marked "d" is 220 m diameter (9.44° N, 268.87° W) and crater marked "e" is 350 m diameter (3.19° S, 326.61° W). High-albedo streaky material at bottom right "f" occurs on slopes exceeding 23°. Distance between boulders labeled "g" (88 m diameter) and "h" is ~770 m (METs = 141204041–141204537; degree annotations (x°) show local slopes at scale of ~300, see Fig. 2 of Thomas *et al.* (2002a) for slope map of entire asteroid).

low gravity, excursions from sphericity, and typically rapid rotation rates (Geissler *et al.*, 1996; Thomas, 1998). Depending on geographic location, and an asteroid's gravity and spin rate, ejecta thickness around a crater rim can easily differ by factors of 2 or more (Thomas, 1998). Additionally, the largest craters, which contribute the majority of material, are not symmetrically placed on an asteroid, thus contributing to non-uniformity of regolith thickness. In addition, on Eros it is now known that downslope movement of regolith is a common regolith process resulting in local variations in regolith thickness (Veverka *et al.*, 2001a; Thomas *et al.*, 2002a). Measurements of geomorphic indicators allow constraints to be put on local thickness, and by combining the average thickness estimates and these local measures a first-order estimates of regolith depth can be made.

Various morphologic estimators of regolith thickness have been discussed in previous studies of the Moon and asteroids. Interior crater morphology and boulder distributions around craters have long been used to estimate the thickness of the lunar regolith above a coherent substrate (Fig. 7). The first estimates of lunar regolith thickness were obtained by

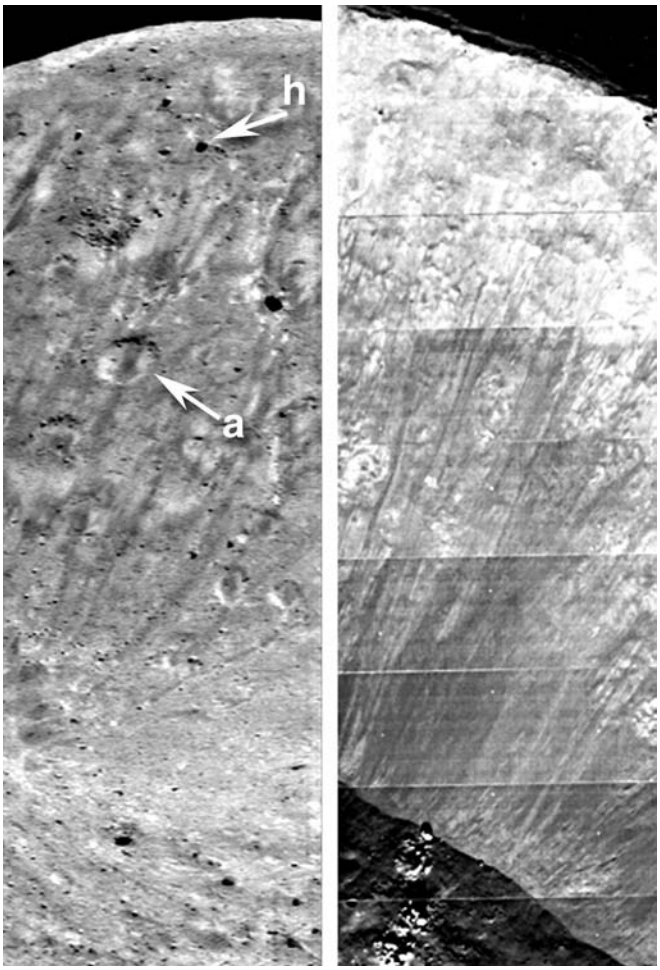

FIG. 13. Eastern wall of Himeros (left–"a" and "h" labeled as in Fig. 12) compared with crater interior on the Moon (right–Lunar Orbiter frame LO5 70 H2, 1280 m width). Note the low-albedo streamers in both cases. In the lunar case the crater wall appears to be much younger (fewer superposed craters) and the wall material forms a sharp boundary with the floor. From *Ranger* descent imaging Shoemaker (1966) proposed that dark and bright streaks seen in lunar craters were the result of downslope slumping revealing higher albedo material from the substrate—the dark streaks were simply remnants of the older preexisting surface between freshly exposed material. However, little work has been done cataloging and investigating mechanisms of formation of lunar crater wall streaks (both higher and lower albedo).

identifying the largest crater with a smooth interior and no blocks and the smallest crater with a blocky rim from *Surveyor* lander images of the surface of mare units (Shoemaker *et al.*, 1968; Shoemaker and Morris, 1968). This transition in crater morphology (no blocks, with blocks) was proposed to represent the point at which craters excavate through the upper layer of loose regolith down to a coherent layer that fractures into blocks that end up as boulders in the interior, on the rim, and in the ejecta blanket. Additionally, concentric crater interior morphology (here referred to as Q&O craters, after Quaide and Oberbeck) observed from high-resolution *Lunar Orbiter* images led to the inference that circumferential interior deposits can be used to determine the depth of an underlying coherent substrate (Oberbeck and Quaide, 1967, 1968; Quaide and Oberbeck, 1968). These early lunar studies generally agreed that on normal mare units the regolith was 1–10 m in depth, excluding areas where large impacts had locally thickened the regolith with ejecta blankets. In the lunar highlands these morphologic indicators are relatively rare, indicating a spotty or incoherent substrate and/or a thicker regolith due to accumulations of ejecta from local craters and distant basins (Cintala and McBride, 1995; Wilcox *et al.*, 2002).

The nearly complete lack of concentric interior morphology (Figs. 6–8) in Eros craters suggests a well-mixed regolith with properties changing gradually with depth to many meters to tens of meters everywhere on the asteroid. We note that Thomas *et al.* (2000) identified a few craters on Phobos that may indicate a lunar-like strength-interface (Fig. 7). This observation may indicate that the regolith on Eros is thicker and/or is characterized by a more gradual transition from loose fragmental material to coherent substrate. As mentioned above, only 3% of Eros was imaged in the better than 2 m/pixel range, thus some small (<20 m) Q&O craters may exist and simply were not resolved. However, with the existing coverage none were found.

The generally rounded, or smooth, morphology of many of Eros' small craters (Fig. 6) is best explained by a widespread layer of loose regolith that infills and drapes the walls and rims and results in a rapid degradation of the craters' original form. This degradation is augmented through impacts, secondary impacts, and seismic shaking. A comparison of the depth of relatively fresh craters to smooth degraded craters indicates an infilling of a few meters to 150 m, with a median at 20–30 m. Large-scale mounds of debris (both boulders and fine-grained material) found in Shoemaker (Fig. 11) and Himeros are up to 80 m tall (Barnouin-Jha *et al.*, 2000). Assuming no underlying topographic structure, the mounds indicate processes that allow 50–100 of regolith to accumulate (Fig. 2). In addition, if pits seen within Eros' grooves are interpreted as drainage features, the regolith could locally be as much 50–100 m thick from the model of Horstmann and Melosh (1989) (Veverka *et al.*, 2000; Thomas *et al.*, 2001). A pervasive covering of loose material would be highly mobile during impact-triggered seismic events, and could erase small craters and partially or wholly bury boulders, resulting in a morphology consistent with that seen on Eros (Fig. 10). Such seismic redistribution of regolith materials has been proposed to explain subdued topography and flat floored craters on the Moon (Schulz and Gault, 1975) and was suggested to be an important process for asteroids (Cintala *et al.*, 1978, 1979). Additionally, as discussed above, it is known that in the lunar highlands, especially in areas of enhanced topography, the number of craters (smaller than 200 m) is diminished relative to the younger mare deposits (Trask, 1969, 1971; Soderblom, 1970; Wilcox *et al.*, 2002). Thus the relative

lack of smaller craters everywhere on Eros (<200 m diameter) is consistent with a pervasive, thick, loose layer of fragmental debris.

Downslope Movement

Downslope regolith movement on Eros forms debris aprons and talus cones, and results in burial of craters and boulders (Veverka *et al.*, 2001a; Thomas *et al.*, 2002a; Figs. 10–13). Debris aprons are found in nearly every crater above 1 km in diameter and are characterized by a relatively smooth and relatively uncratered texture (at 1–5 m/pixel), sharp margins at the bottom of some of the slopes, and in some cases uphill mounding behind obstacles, and striations caused by subsequent downslope movement of boulders. The debris aprons infill superposed craters (allowing thickness estimates) and buries preexisting topography in the bottoms of craters. These relationships show they form as a secondary process from material that is mobilized from outside the crater and spills over the rim in gravity flows well after the original crater was formed.

Where slopes exceed 25° relatively fine-grained material generally show higher albedo (than avergae Eros materials) and from smooth deposits on crater walls (Figs. 14 and 15). The higher albedo smooth deposits are found in heavily degraded craters burying or embaying interior topography and evidently represent a secondary process. Albedo contrasts between the higher albedo deposits and substrate are typically on the order of 1.5 (Fig. 15; Table 3) (Clark *et al.*, 2002; Bussey *et al.*, 2002; Thomas *et al.*, 2002a). These higher albedo deposits also show a slight increase in 550/760 nm ratio of about 1–2% and in the 950/760 nm ratio an increase of about 5–8% (values listed for interior of Psyche crater mission elapsed times (METs) 143945337 to 143947883; see also Murchie *et al.*, 2002b). Both the MSI color results and the NIS spectral data have lead to the interpretation that the high-albedo smooth deposits represent a material that is less space weathered than average Eros (Murchie *et al.*, 2002b; Clark *et al.*, 2002). Clark *et al.* (2002) proposed that the high-albedo streaks found in Psyche crater resulted from slumping of a surficial material exposing higher albedo material from the substrate. This explanation is simple, requiring no special mechanism other than seismic shaking or thermal creep to cause material to move down slope revealing a substrate that exhibits a higher albedo because it has undergone little to no space weathering.

In numerous instances (Figs. 14 and 15) lower reflectance (relative to average Eros) deposits are found at the downslope termination of the higher reflectance wall-hugging deposits. It is not certain that in all cases these lower reflectance materials are actually lower reflectance than average Eros, or simply appear so due to photometric effects resulting from uncorrected variations in local topography (Fig. 15; Table 3). The lower reflectance deposits are found in numerous craters at many lighting and viewing geometries suggesting strongly that they are real. Additionally, it is found that some lower reflectance deposits exhibit unique color ratio values (see discussion

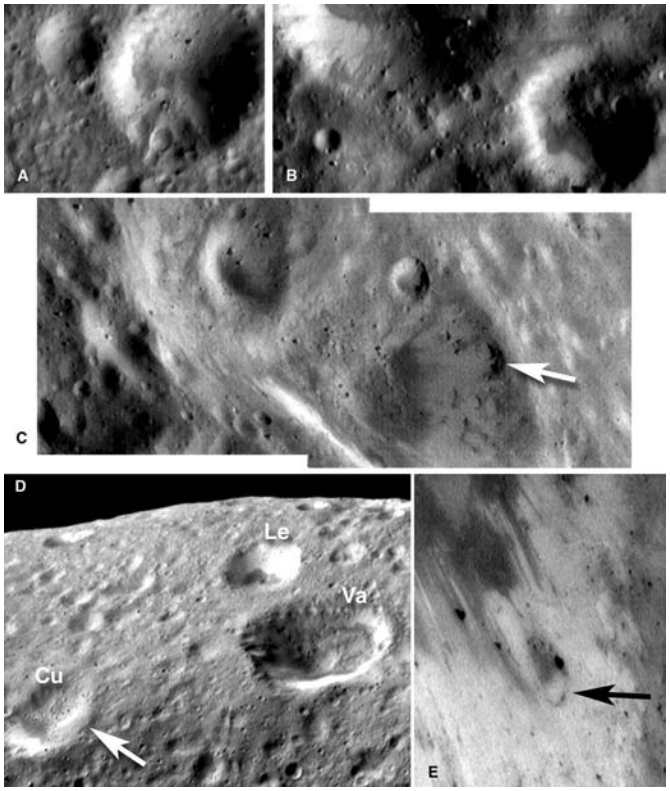

FIG. 14. High-albedo smooth deposits are commonly found on walls of craters that exceed slopes of about 20–25° (Thomas *et al.*, 2002a; Murchie *et al.*, 2002b). Due to Eros' grossly non-spherical shape large slope differences commonly exist from one side of a crater interior to the other, resulting in the semicircular shapes of many of the higher albedo wall deposits (see Figs. 2 and 3 of Thomas *et al.*, 2002a). (a) Crater Mahal 79.1° N, 172.1° W, 950 m diameter; the north pole is just off image upper left corner (MET = 132584452). (b) Large crater partially seen at upper left is Dulcinea (76° S, 273° W, 1.5 km diameter). Smaller crater (~890 m diameter) at right, like Dulcinea, is heavily degraded, yet the higher albedo smooth deposits are craterless at this scale, thus indicating their relatively young age. Small sharp crater at lower left is ~150 m diameter, Eros' south pole is just off the frame, below the "B". (MET = 141011290, see Fig. 10c for context). (c) Oblique view of interior of Tai-yu crater (1.4 km diameter) showing high-albedo smooth deposits burying preexisting superposed craters. Buried crater (arrow) is 220 m diameter indicating 10–20 m thickness of deposit (METs = 155806311–155806371). (d) Leander (Le) is one of the few craters on Eros that exhibits a nearly symmetrical high-albedo deposit. Here (7.97° N, 230.74° W, 1.7 km diameter) the preexisting topography had a low slope; this condition allows steep slopes around the entire interior perimeter of the crater. Also note the orthogonal corner of Valentine (Va) crater suggesting underlying structural control during crater formation (METs = 130904029, 130904091, 130904153, 130904215). Lower albedo material is found at the base of the higher albedo material in all three craters (Leander, Valentine, Cupid). (e) Finely interfingered high- and low-albedo streaks inside Selene crater (14° S, 12.5° W, 3.5 km.). Nearly buried crater (arrow) is ~180 m diameter, its amount of fill suggests 10–20 m of overlying material (METs = 155816571–155816871).

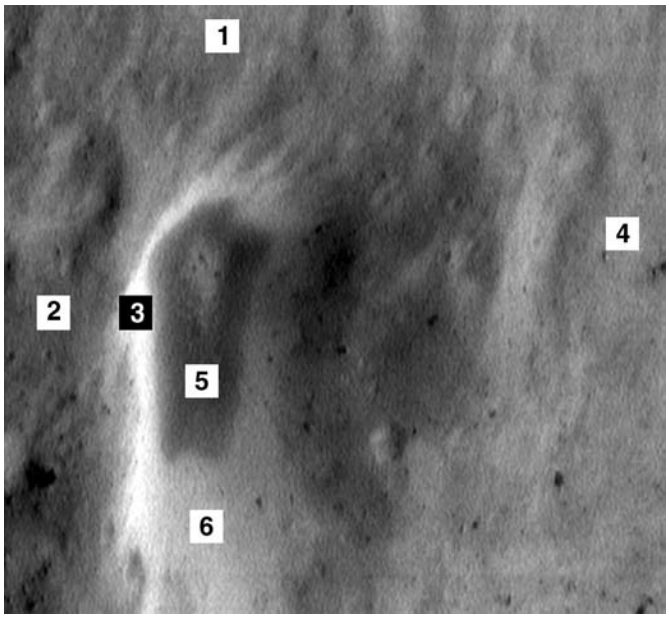

FIG. 15. Interior of Avtandil crater (22.5° S, 233.1° W, 1.2 km diameter), boxes indicate sample regions where calibrated pixel values (I/F, not normalized for topography) were averaged (see Table 3 for data values). Note that the high-albedo smooth wall deposits completely coat the interior of the upper (steep) crater walls. In this area of the asteroid, the local surface is generally parallel to the local equipotential so the crater walls have roughly the same gravitational slope symmetrically about the interior of the crater; this situation is not the norm on Eros (MET = 155810691).

below). Such lower reflectance deposits may represent important clues to the origin of the higher reflectance smooth deposits. Perhaps as average Eros regolith moves downslope lower reflectance grains preferentially slide to the bottom, while higher reflectance grains cling to the slopes. Mechanical separation of grains by composition is not unknown. On the Moon, lower reflectance material found in valleys and draws between massifs north of the *Apollo 17* landing site are proposed to represent the preferential downslope movement of a mafic component of the regolith (Lucchitta, 1972; Robinson and Jolliff, 2002). Grain separation on Eros has been proposed to explain the anomalous color (Robinson *et al.*, 2001) and geochemical properties (Evans *et al.*, 2001) of the unusual ponded deposits (which show similar color trends to the high-reflectance streaks), and a related mechanism may be at work here. Obtaining accurate photometric corrections of these deposits in craters smaller than Psyche is problematic given the limited resolution of the current shape models (Thomas *et al.*, 2002a; Zuber *et al.*, 2000). Future digital analysis of high-resolution topography from MSI stereo pairs should resolve this issue.

Downslope movement of regolith is also seen in the form of lower reflectance streamers on some steep slopes (Fig. 12). The longest streamers, over 2 km, occur on the eastern side of Himeros on slopes of about 5–25°. Are these streamers actually lower reflectance relative to average Eros materials or are they

TABLE 3. Reflectance values (760 nm) for sample areas shown in Fig. 15.

Sample box	Average	Standard deviation	$n \times n$	Average/ sample 4b
1	0.0649	0.0026	9	0.91
2	0.0536	0.0021	9	0.75
3	0.1099	0.0060	9	1.54
4a	0.0737	0.0024	9	1.04
4b	0.0712	0.0033	51	1.00
5	0.0484	0.0035	9	0.68
6	0.0887	0.0035	9	1.25

Samples 4a and 4b have the same center with differing box sizes.

simply average Eros material superposed on higher reflectance patches? After photometric normalization to standard geometry of 30° incidence and 0° emission angles (see details in Bussey *et al.*, 2002) the streamers have 950 nm normalized reflectance (I/F) values 5–15% below that of average Eros (0.11, at 950 nm; Bussey *et al.*, 2002). The higher reflectance materials on the same wall of Himeros typically have normalized 950 nm I/F values 15–30% greater than that of average Eros. The lower reflectance materials may indicate a difference in photometric functions from surroundings or may result from grain sorting (Thomas *et al.*, 2002a). At high resolution, portions of these forms follow small furrows, and even include some sinuous troughs of order 2 m in depth (see also images in Thomas *et al.*, 2002a). The streamers indicate that material is mobilized from regions on the rim or outside of Himeros and flows down the steep slopes contributing to sediment deposits on the gravitational floor of Himeros.

Smaller sinuous troughs, only about a centimeter deep, are visible in the last few images taken during the descent to the surface (Veverka *et al.*, 2001b). Possible mechanisms for this style of erosion and transport are as yet not well defined. These small vertical scales, in a gravity of less than 1/1000th that on the Earth, indicate the processes may not have ready analogies from the Moon or Earth.

Boulders

Eros is littered with more than 10^4 boulders larger than 10 m in diameter (Thomas *et al.*, 2001) representing the extreme of the large end of particle size distributions in the regolith. Their morphology ranges from angular to fractured to disaggregated (Fig. 16; Table 4). In at least one case, a large irregular angular boulder (>100 m diameter; Fig. 16b) exhibits overhangs. Apollo astronauts found similar overhangs on lunar boulders. Probably the best known example is "shadow rock" at the *Apollo 16* landing site (AS16-106-17413-17415; Dietrich and Clanton, 1972). Most boulders on Eros were probably emplaced as low-velocity ejecta from crater-forming events. Their current morphologic state is most likely influenced by three key factors

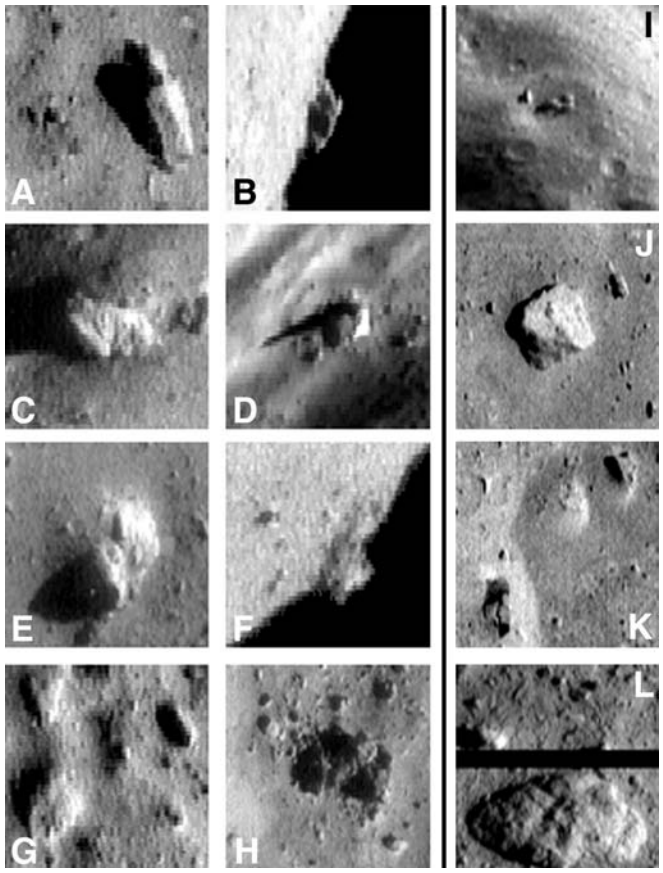

FIG. 16. (*left*) Boulders on Eros exhibit a wide spectrum of physical properties (a–h) from sharp angular coherent boulders to disintegrating loosely bound rubble piles (Table 4). We interpret this range of coherence to reflect variations of coherence with depth in the Eros regolith. (i) Grouping of 60–80 m diameter boulders (inside 1000 m diameter degraded crater); see oblique view in upper left of Fig. 12. (j) Angular 36 m boulder. Square shapes of boulders may indicate an organized joint pattern inside Eros consistent with a relatively intact interior. (k) Fractured boulder at lower left is ~20 m long; this example is reminiscent of boulders investigated on the Moon by Apollo astronauts. The fracturing of the lunar boulders was thought to have occurred as the boulder impacted at relatively low velocities as a secondary—the same is most certainly true for the Eros example shown here (and many others). (l) Rounded, partially buried 16 m (left to right) boulder showing fractures (or joints) spaced ~1 m. The black stripe across framelet represents data lost in transmission (–40.7° S, 275.7° W; Table 3 for relevant image parameters).

(in order of importance): original coherence of the material composing the block, impact velocity, and exposure age on the surface. The original strength of boulder material is controlled by impact fracturing and lithification history prior to the event that dislodged and deposited it in its current location. Meteorite specimens show that breccias form on asteroids (Wahl, 1952; Keil, 1982; Bunch and Rajan, 1988; and many other references found within) from material disaggregated by impact(s) forming a loose regolith. This material is subsequently buried and heated (in some cases partially melted) to form a lithified breccia that is subsequently ejected and delivered to the Earth. It is unlikely that loose regolith (pre-metamorphism) could survive ejection and entry to the Earth; thus this material is not represented in the meteorite samples. It is reasonable to assume that some portion of Eros' regolith have been heated to different degrees, during impact events, to form a range of consolidation states (from loosely aggregated to completely lithified) within the upper loose, fragmented portion. During subsequent impact events material is excavated from various depths and the ejected material has a range of internal strengths (from loose regolith to well-lithified breccia to original coherent bedrock). Thus, the morphology of the blocks most likely represents a spectrum of initial internal strength of the ejected material.

Well-cemented breccias or original coherent bedrock should form sharp angular blocks; fractured breccias and fractured bedrock would account for fractured boulders, while poorly to unlithified regolith may appear as disaggregated clods. Exposure to micrometeorite bombardment would tend to wear down sharp edges and eventually disintegrate boulders over

TABLE 4. Relevant parameters for Eros boulders shown in Fig. 16.

Letter	Mission elapsed time	Latitude	Longitude (W)	Radius of boulder (km)	Diameter of boulder (m)
A	156082816	10.13° S	5.27°	13.62	54
B	138852654	2.11° N	341.85°	11.857	129
C	155895391	6.03° S	30.76°	15.16	50
D	139808336	28.72° N	74.89°	3.64	90
E	155982204	4.01° S	186.35°	16.04	49
F	155823471	78.21° S	220.61°	6.46	100
G	147951938	56.05° S	326.10°	6.91	45
H	155987742	8.82° S	3.33°	13.79	91
I	130178931	10.43° N	253.79°	8.06	100–150
J	157415228	54.04° S	238.10°	6.32	36
K	157415638	47.38° S	250.28°	6.59	20
L	157416613	40.70° S	275.70°	6.57	16

time at varying rates proportional to the original coherence of the block and time spent on the surface. The impact velocity of a boulder (>0 to <17 m/s; Veverka *et al.*, 2000) will affect the amount of disaggregation to some degree (Fig. 16). There are several cases of boulders that appear to have fractured *in situ*, either at the moment of impact or later by a small high-velocity impactor.

The observation that many large and small boulders (up to ~150 m diameter) exhibit sharp and angular facets signals that at least some of the interior of Eros contains competent material at the 100 m scale (or greater), ruling out the possibility that Eros is composed entirely of loosely aggregated fine-grain material. The interpretation that at a resolution of 5 m/pixel or greater only one crater (Shoemaker) has produced an abundant population of boulders (including the majority of boulders on the asteroid above 15 m diameter, n = 6760; Thomas *et al.*, 2001) argues that much of the near-surface portions of the asteroid are highly fragmented and that joints or fractures inhibit formation of abundant blocks on scales larger than several meters. Shoemaker crater (7.6 km in diameter) appears to have been formed on a preexisting rim of Himeros and probably excavated to a depth of >300 m, down to a more coarsely fractured zone allowing the generation of a suite of block sizes ranging from a few meters up to 150 m.

Reimpacting ejecta can give insight into local regolith characteristics. Tracks of rolling or bouncing boulders are rare on Eros, less than five having been positively identified (Prockter *et al.*, 2002; Robinson *et al.*, 2001). Nor are they common in lunar craters. One of the few examples of bounce marks on Eros provides useful quantitative information on the regolith. The image (Fig. 17) shows a boulder, ~35 by 50 m horizontal dimensions, that has produced a furrow about 150–160 m in length and 45–50 m in width, then skipped ~200 m, and made another furrow ~50 m in length before coming to rest. The first furrow has a hint of a raised rim, and in another image (136607730) the depth of the furrow can be estimated from shadows as being 8–15 m. The furrow proves that the boulder pushed loose material aside during its grazing impact. The boulder was probably traveling substantially <10 m/s, the escape velocity in this region of Eros. In this low-gravity, low-velocity regime, the whole traverse from initial contact to final stop, ~350 m, would have taken at least 50 s: little slowing over the 200 m bounce, and an average velocity of <5 m/s over the length of the furrows (length of deceleration). The most important point is the direct evidence of at least 10 m of loose surficial material required to allow the furrow to form. The furrow is found in a rather average hilly intercrater area of the asteroid—not in a sediment trap. It appears that even in this region the regolith is at least 10 m thick.

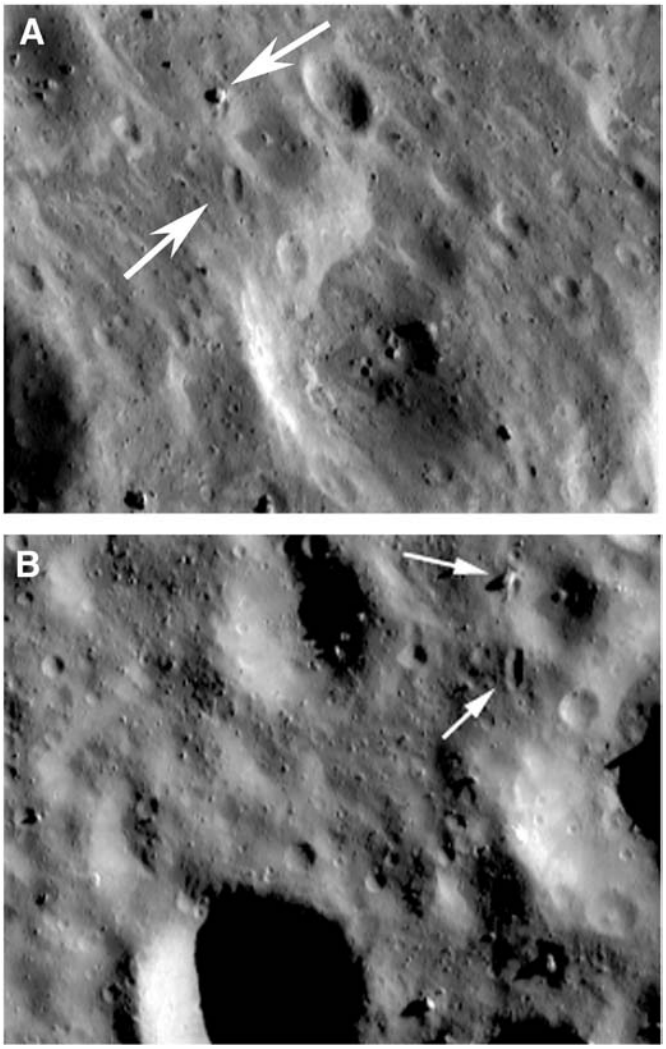

FIG. 17. (a) Low-angle, low-velocity secondary impactor (upper arrow) carved a 50 m wide furrow (lower arrow). Large degraded crater in center bottom is ~780 m diameter (1.8° S, 212.9° W; MET = 138525395, frame width ~1630 m; see also Fig. 14 of Prockter *et al.*, 2002). (b) Same boulder and furrow as in (a) from different viewpoint with lower Sun angle. The crater with heavily shaded interior partially off bottom of frame is ~730 m diameter centered at 3.41° S, 218.9° W (MET = 136607730, frame width ~2050 m).

Ponds

Craters with distinct planar bottoms on Eros were first identified in very high-resolution images (better than 1 m/pixel) obtained during a LAF on 2000 October 25 (Figs. 18 and 19; Veverka *et al.*, 2001a; Cheng *et al.*, 2001). These initial analyses presented arguments that the planar bottoms were formed as a result of secondary infilling of craters (Veverka *et al.*, 2001a) or the expression of an interface between a fragmental layer and a coherent substrate (Cheng *et al.*, 2001). Veverka *et al.* (2001a) noted that the flat bottoms often do not correspond to the geometric center of the host crater and are offset in a direction towards the downslope side of the crater. These key observations lead to the argument that fine-grained material flowed into the craters and *ponded* to a local equipotential (Fig. 18). In the extreme case ponds are observed on the upper

walls of craters in areas where the local gravity vector is far from perpendicular to the surface (near the long ends of asteroid; Veverka *et al.*, 2001a) discounting the possibility that ponds express an interface of a loosely bound regolith over a competent substrate. Additionally, morphologically fresh ponds are found in heavily degraded craters, requiring that they are not a primary feature of the crater. Direct evidence that the pond material is only loosely bound and not coherent (as would be found in a

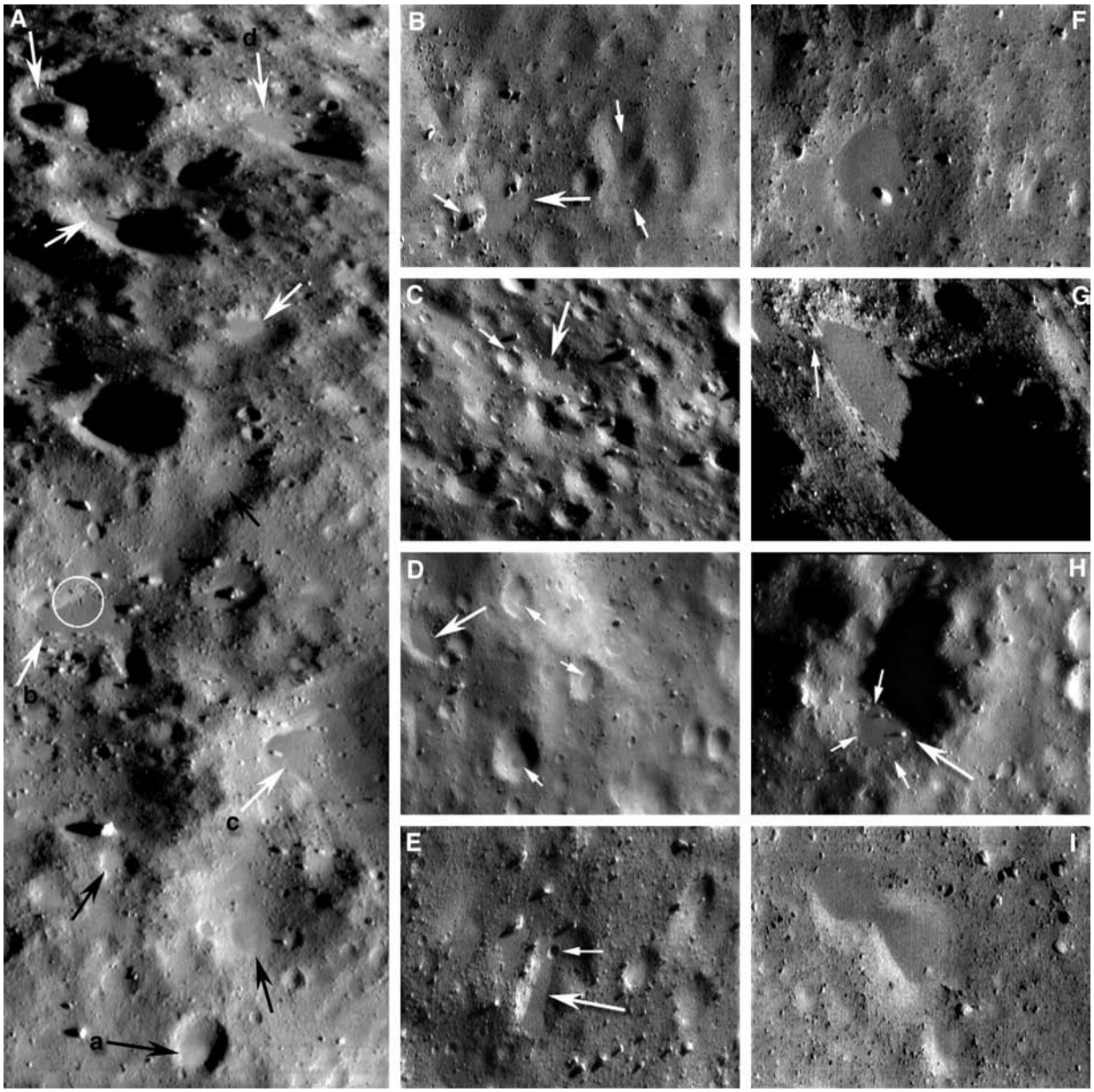

FIG. 18. (a) Mosaic spanning ~7° of longitude (166° to 173° W top to bottom) roughly between 2° and 4° S, showing an area of efficient pond formation. Large arrows indicate well-formed distinct ponds, while black arrows show ponds with diffuse boundaries. Circle locates groove in pond excavated by low-angle impactor seen just off pond surface (see detailed discussion in Robinson *et al.*, 2001). Pond labeled "A" is contained within 30 m diameter crater centered at 2.75° S, 172,6° W. Pond "D" is ~190 long side (detailed view of "D" see Fig. 1d of Robinson *et al.*, 2001). Pond "F" is ~130 m diameter, 4.0° S, 166.5° W (METs = 154461105–154460905). (b) Pond flooding irregular topographic low, note also nearby boulders with prominent fillets; the pond length is ~90 m (MET = 147953757, 14.8° S, 35.6° W). (c) Pond with arrow is 125 m long. Also note small pond perched on crater rim, just to the left of arrowed pond (MET = 152448816, 6.6° S, 8.3° W). (d) Ovoid shape pond in upper left is ~120 long (MET = 154258195, 3.8° S, 181.0° W). (e) Pond formed in linear trench (MET = 155888689, 2.8° S, 182.5° W; long axis of pond from sharp-rimmed crater to bottom margin ~70 m). (f) Pond diameter is 80 m; note the prominent fillet seen around the boulder embayed by the pond. Fillets around boulders are common on Eros and are probably formed by accumulation of fine material impacting boulder and rolling down slope (MET = 156083231, 5.9° S, 19.1° W). (g) Large pond that embays (arrow) nearby blocky region (MET = 156087486, 3.9° S, 166.5° W, ~230 m frame width, see pond marked "A" in Fig. 18 for context). (h) (MET = 157353946, 0.5° S, 174.6° W, ~900 m frame width). (i) Pond viewed at extremely high resolution (26 cm/pixel) during *NEAR Shoemaker* descent to the surface (MET = 157416028, 45.83° S, 262.59° W, ~140 m frame width).

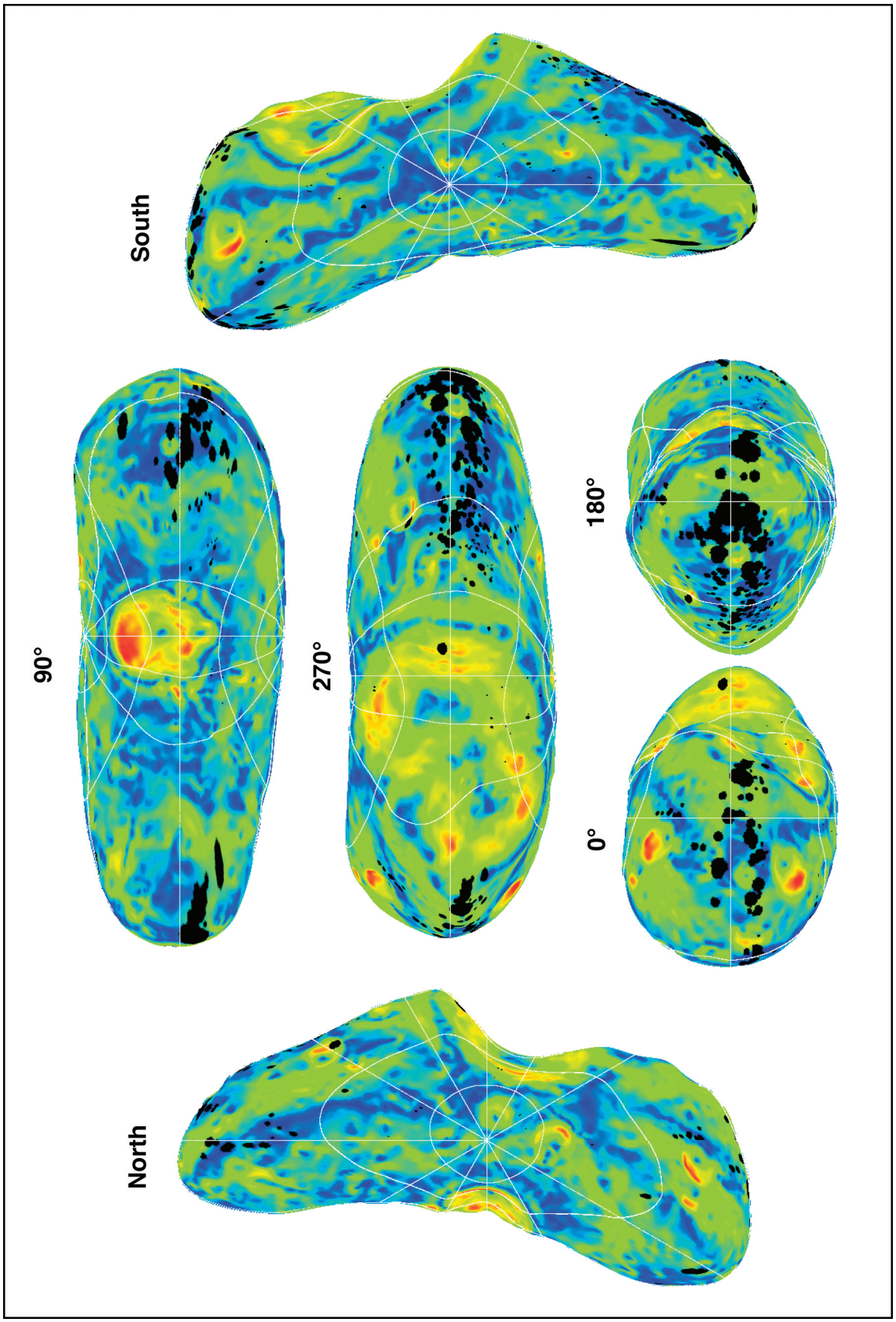

FIG. 19. Ponded deposits (black) are found preferentially in Eros' equatorial belt. Sizes of pond symbols (black) are proportional to pond sizes, not actual size. The ponds are superposed on slope values; warmer colors represent increasing slopes (0–36°; see Thomas *et al.* (2002a) for details of shape model). Latitude longitude grid increment is 30°.

solidified impact-melt pond or a planar exposure of bedrock) comes in the form of gouges made by low-velocity, low-angle impactors (Fig. 18; see also Fig. 1 of Robinson *et al.*, 2001) and small (several centimeter width) valleys interpreted to indicate draining of pond material into voids (Veverka *et al.*, 2001b).

The extreme smoothness of the ponded deposits has no known analogs on other airless bodies, but image data of comparable resolution (~1 m/pixel) exist for only Phobos and the Moon. No analogous ponded deposits have been identified on Phobos in published work (Thomas *et al.*, 2000) and our examination of Mars orbiter camera (MOC) images of Phobos have revealed no planar or flat floored craters similar to ponds found on Eros. Lunar crater morphologies were cataloged from high-resolution Lunar Orbiter images (1 m/pixel and better) in a series of papers (see discussion above; Oberbeck and Quaide, 1967, 1968; Quaide and Oberbeck, 1968). These studies reported four distinct morphologies (Q&O craters) for small mare craters, related to an interface between a regolith and a coherent substrate—none of these morphologies is similar to the ponded deposits found on Eros (Figs. 5, 6 and 18). We have reexamined over 100 Lunar Orbiter III and V high-resolution frames (better than 1 m/pixel with incidence angles generally ~70°) specifically looking for analogous morphologies within lunar craters and have found none. Ponds are not the result of crater formation, but rather form later through a secondary process.

In most cases ponds occur within craters where there is no obvious inflow of material, thus implying an interior source. Extreme cases are found in pond-bearing craters that are perched on local topographic highs (see Fig. 1 of Robinson *et al.*, 2001). Is it reasonable to assume that a pond can be formed with materials mobilized solely from within the source crater? We can estimate the amount of material forming a pond based on the size of the enclosing crater, the mean diameter of the pond, and the estimated depth of craters in the absence of ponds. A parabolic crater profile with depth 0.15 that of the diameter can be assumed from the depth/diameter measurements reported above (Fig. 9). The volume of the pond deposit is then calculated from the diameter of the pond and the assumptions on crater shape. The volume of the pond divided by the area of the enclosing crater gives the depth of material that has been accumulated from the slopes of the enclosing depression. This calculation assumes a similar density for the slope material and for the ponds, yet they may be significantly different. The pond material is probably size sorted, and could conceivably have a greater porosity than regolith on the crater slopes. The average depths of the source areas for the ponds are shown as a function of latitude in Fig. 20. The first important result of this analysis is that very little material needs be removed from interior slopes of a host crater to form a pond, usually <20 cm. The depths might be less if the ponded deposits have increased porosity. The second result is the concentration of greater source depths, in equatorial regions (Figs. 19 and 20), suggesting more efficient pond formation mechanisms in these areas of the asteroid.

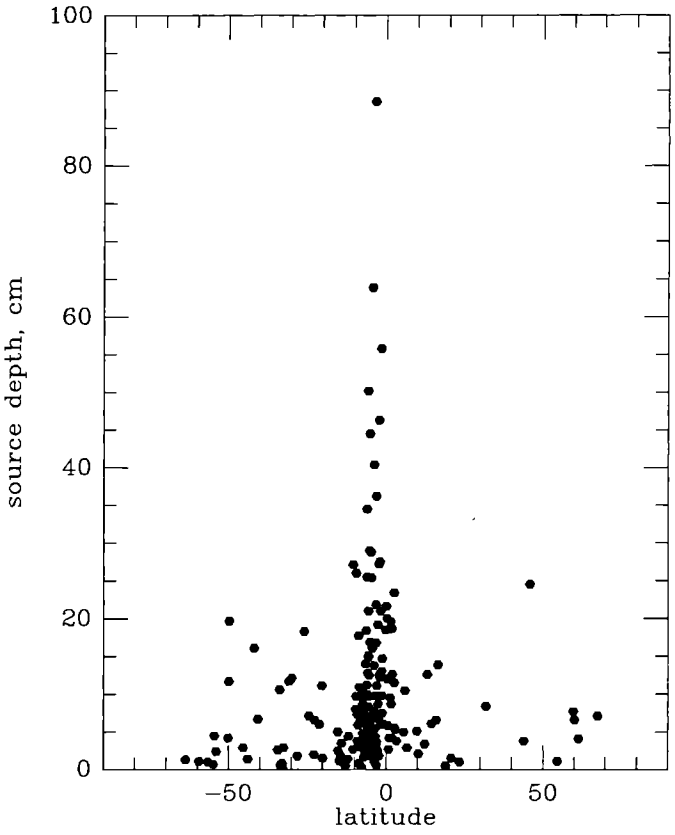

FIG. 20. Calculated source depth of materials making ponded deposits within craters. Volume of ponded materials is estimated from its fractional size of the enclosing combined with assumptions about the crater depth profile. This volume is then divided by area of the crater; see text for details.

High-resolution multispectral images have shown that ponds have color properties distinct from their surroundings (Robinson *et al.*, 2001): ponds are less red ("bluer") and have an enhanced 1 μm band ratio (Figs. 21–23; Tables 5 and 6). The unique color properties of the ponds are potentially important clues to the mechanism of formation. In the lunar regolith, as fresh crystalline material is altered by exposure to the space environment (space weathering), it becomes darker and redder and the mafic absorption feature near 1 μm is diminished (McCord and Johnson, 1970; McCord and Adams, 1973). This optical alteration is attributed to submicroscopic metallic iron vapor deposited on grains, the vapor resulting from micrometeorite impact and solar wind sputtering (reviewed in Hapke, 2001; Pieters *et al.*, 2001). Also important is the formation of relatively large aggregates of quenched melt and adhering regolith particles, called agglutinates, which tend to darken lunar soils. There is considerable debate over the rates at which space weathering (including agglutinate production) takes place in asteroid regoliths (Matson *et al.*, 1977; Hapke, 2001; Pieters *et al.*, 2001). In the case of lunar-like space weathering the ponded material would correspond (on the basis

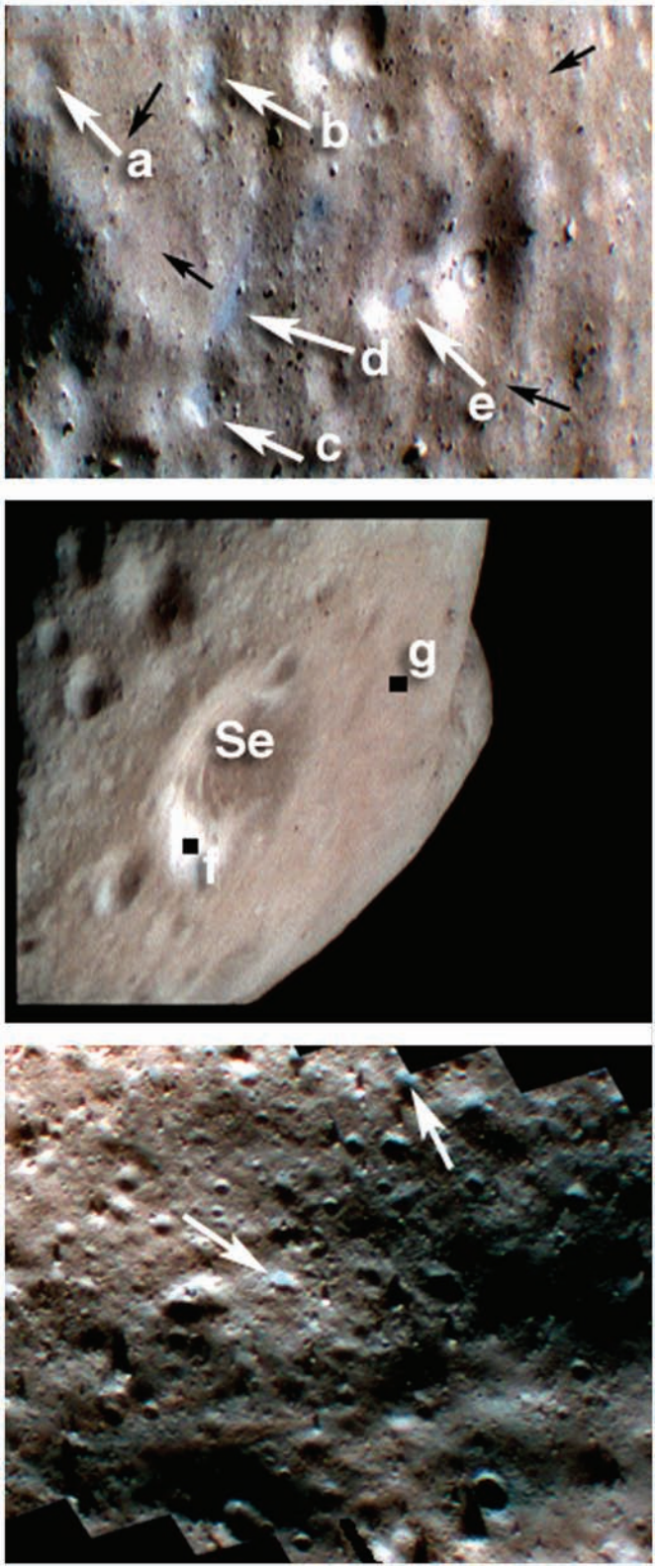

FIG. 21. *(Left)* (top) Ponded sedimentary deposits ("ponds") on Eros exhibit distinct color properties relative to their surroundings; in this saturation stretch color ponds show up as smooth blue deposits occupying topographic lows. At the center of the frame incidence angle is 47° and the phase angle is 86°. Located at latitude 9.8° S, longitude 32.4° W). Spectral samples of each pond (white arrows indicate sampled ponds "a" 3 × 3 pixel sample, "b–e" 5 × 5 pixel samples) and surrounding intercrater terrain (black arrows, 9 × 9 sample boxes—see also Figs. 22, 23 and Table 5; METs = 154760995F1, 154760999F3, 154761001F4, width of frame 1.13 km). (middle) Ponds share color properties with high-albedo patches found on many steep crater walls. In this oblique view of Selene crater (3.1 km diameter) spectral sample areas are marked with black boxes, "f" is 9 × 9 pixel average while "g" is a 51 × 51 pixel average (see Fig. 23; Table 5; METs = 151926384F1, 151926386F3, 151926388F4). Here the ponds show a ~6% reflectance contrast (top panel) with their surroundings while the bright material in Selene exhibits a 60% increase in reflectance relative to the surrounding terrain. (bottom) Shoemaker Regio was probably formed as a result of fallback material during the formation of Shoemaker crater with subsequent remobilization by downslope movement events (see Fig. 11a–c). Despite the abundance of regolith materials, ponds do not form efficiently in this environment, perhaps due to the predominance of steep slopes and relatively frequent reworking of materials? However, small ponds (arrows) can be found in high-resolution images and they share the same color properties (Fig. 23) as ponds found elsewhere on Eros (METs = 155091985F1, 155091987F3, 155091989; distance from arrow-tip to arrow-tip 770 m, lower pond located at 19.32° S, 309.60°). In all three panels colors formed as red 950 nm, green 760 nm, and blue 550 nm.

of relative color) to less altered material (relatively immature or fresh); surrounding materials would be more altered (relatively mature).

Changes in grain size and packing affect the color properties of silicate materials (Adams and Filice, 1967). For mafic rocks, as grain size decreases, color becomes *redder* at visible wavelengths. However at very fine-grain sizes (<50 μm) some mafic materials reverse this trend and their visible color becomes bluer (Adams and Filice, 1967). To explain the color properties of the ponds by differences in grain size alone, sorting and transport of an extremely fine-grain component (<<50 μm) of the regolith is required.

Pond color properties have been attributed to a sorting process that preferentially removes silicate grains (olivines and pyroxenes) from a silicate-plus-metal regolith and deposits them in topographic lows to form silicate-enriched (or iron metal depleted) ponds (Robinson *et al.*, 2001). Such a hypothesis is testable by comparing the total iron content of ponds with that of average Eros. After *NEAR Shoemaker* successfully landed on a ponded deposit its GRS was used to measure the surface composition revealing a depletion of total iron relative to the average surface of Eros. This apparent iron depletion at the landing site pond is consistent with ponds being formed from such a compositionally sorted sediment (Evans *et al.*, 2001). What is the mechanism that drives the putative grain segregation? Seismic redistribution of fine material to form the ponds was considered by Robinson *et al.* (2001), but the geographic distribution and color properties of the ponds was

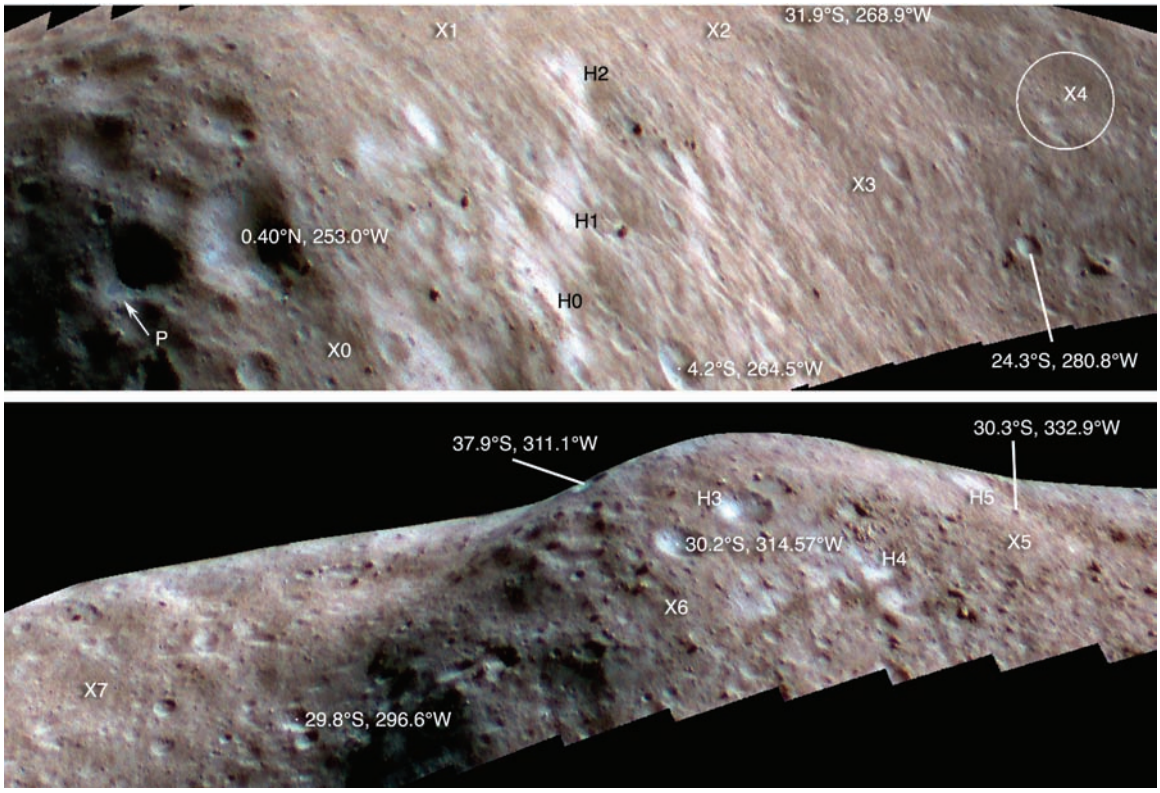

FIG. 22. (top) Color composite of southeast edge of Himeros crater. Labels indicate locations of spectral samples plotted in Fig. 23b, see Table 6 for data values (P = pond location, Xs = intercrater normalization areas, H = higher albedo steep topography materials, latitudes and longitudes mark crater centers; resampled point perspective mosaic, north generally towards bottom of mosaic). The *NEAR Shoemaker* spacecraft landed within the circle, most likely near the lower left of "X4". (bottom) Ridge in center of this point perspective mosaic is the southeast rim of Shoemaker crater; Himeros is to the left (approximately east) and Shoemaker is to the right (approximately west). Data in both panels (METs = 147088209–147093109) were acquired on 2000 October 16 as part of a longitudinal mosaic (~20° latitude) wrapping around the entire asteroid. Annotations same as in top panel (Fig. 23b; Table 6), in both panels colors are formed as red 950 nm, green 760 nm, and blue 550 nm.

TABLE 5. Color data (reflectance) located in Fig. 21 and presented in Fig. 23a.

Figure/Location	Sample	550 avg	550 std	760 avg	760 std	950 avg	950 std	550/760	950/760	*n*
Fig. 21 Top	a	0.042	0.000	0.057	0.001	0.053	0.001	1.065	0.927	9
Fig. 21 Top	b	0.045	0.001	0.062	0.002	0.058	0.001	1.049	0.935	25
Fig. 21 Top	c	0.045	0.001	0.061	0.002	0.057	0.001	1.063	0.928	25
Fig. 21 Top	d	0.044	0.001	0.060	0.002	0.056	0.001	1.072	0.931	25
Fig. 21 Top	e	0.048	0.001	0.065	0.001	0.060	0.001	1.071	0.928	25
Fig. 21 Top	bl1	0.038	0.002	0.055	0.003	0.055	0.003	0.999	0.996	441
Fig. 21 Top	bl2	0.041	0.002	0.058	0.003	0.058	0.002	1.017	0.990	441
Fig. 21 Top	bl3	0.040	0.001	0.059	0.003	0.059	0.002	0.995	1.004	441
Fig. 21 Top	bl4	0.036	0.002	0.052	0.004	0.052	0.003	1.001	1.004	441
Fig. 21 Middle	f	0.087	0.003	0.117	0.005	0.110	0.003	1.046	0.931	441
Fig. 21 Middle	g	0.055	0.002	0.078	0.003	0.077	0.002	0.999	0.987	81
Fig. 21 Middle	g-large	0.056	0.003	0.079	0.004	0.080	0.003	1.000	1.000	2601
Psyche	far bright	0.060	0.003	0.083	0.004	0.080	0.003	1.034	0.954	169
Psyche	average	0.042	0.001	0.060	0.003	0.060	0.002	1.000	1.000	169
Psyche	near bright	0.080	0.003	0.110	0.004	0.102	0.003	1.052	0.927	169
Psyche	darker	0.027	0.002	0.041	0.002	0.044	0.002	0.955	1.064	81

Samples labeled Psyche not shown in Fig. 21 (Psyche bright = higher reflectance wall deposits, Psyche average = intercrater normalization area, Psyche dark = lower reflectance material at base of Psyche bright materials). Ratios normalized to the median of the intercrater units ("blx"s black arrows for Fig. 21 top panel and sample "g" for Fig. 21 middle panel). Sample areas "g" and "g-large" are centered at same spot to demonstrate insensitivity of normalization areas to local color variations; the difference between the small and large box is <2%.

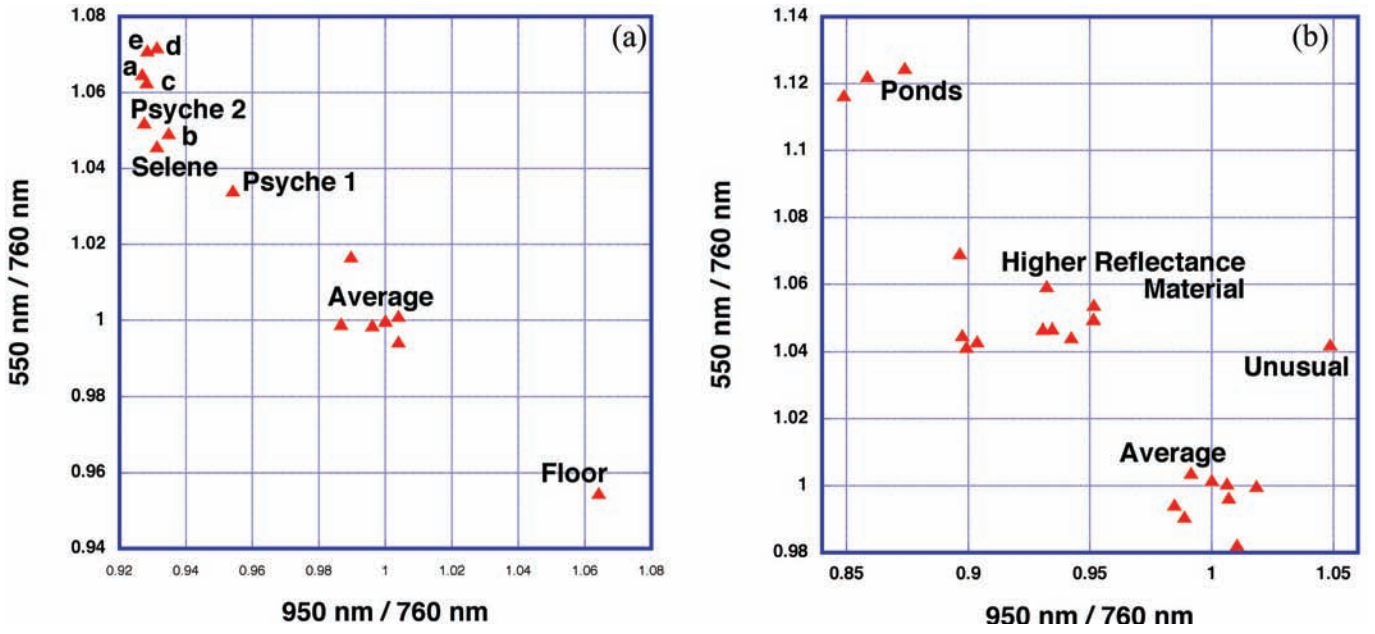

FIG. 23. (a) Points labeled "a–e" correspond to ponds labeled in Fig. 21 top panel. Points labeled Selene (Fig. 21 middle panel, point "g") and Psyche 1 and Psyche 2 correspond to higher reflectance wall deposits in those craters. The point labeled "Floor" corresponds to lower reflectance material at the base of brighter wall material inside Psyche (130111937F1, 130111939F3, 130111941F4; not shown). The lower reflectance Psyche Floor material was first identified in Murchie *et al.* (2002b) and is illustrated in their Fig. 19b. The data shown here are consistent with a two component mixing line, endmembers are represented by relatively high visible ratio and low near-infrared ratio (upper left of plot: pond samples "a–e", Psyche and Selene higher reflectance materials) to low visible and high near-infrared ratio (lower right of plot: Psyche Floor). Data are normalized to median of intercrater areas "Average Eros" from each frame set (respectively), since there is one intercrater area each for the Selene and Psyche color sets both normalization areas plot at 1,1. (b) Color ratio values from Himeros–Shoemaker mosaics shown in Fig. 22 (see also Table 6). An unusual patch of material "Unusual" found in crater marked 4.2° S in Fig. 22 (Table 6) falls off the putative mixing line seen in (a). This deposit may represent a new spectral unit, further analysis of high-resolution color sequences is needed to understand the significance of this material.

not easy to reconcile with such a mechanism. Robinson *et al.* (2001) noted that the near-equatorial region, where ponded deposits are most abundant (Fig. 19), experience extended times near dawn or dusk, an environment potentially favorable to electrostatic charging (Lee, 1996). This general correspondence of pond location and lighting conditions led Robinson *et al.* (2001) to propose that electrostatic levitation with subsequent transport and redistribution of the finer fraction of the regolith results in pond formation. Lee (1996) modeled the possibility of such a process on asteroids and found that only the finest components (<100 μm) could be levitated (finest particles or possibly fine particles with little to no iron metal). Such a model is also consistent with the characteristic color properties of the ponds.

The electrostatic model has not been worked out in detail, nor has it been extended to cover the sedimentologic processes that would occur between lifting particles and collecting them in a deposit. Such processes most likely need to account for shadowing and some period of mutual repulsion of the particles of a strength that allows settling to a potential surface. That is, the grains would be largely influenced by gravity, but unable to immediately stick to one another because of electrostatic repulsion while settling in topographic lows.

A comparable lighting environment to that which occurs in the equatorial regions of Eros occurs near the lunar poles. Extreme examples exist near the lunar south pole where some massifs are illuminated at grazing incidence angles for >80% of a lunar year (Bussey *et al.*, 1999) and nearby depressions may be permanently shadowed (Arnold, 1979). The highest resolution image data for the lunar poles was acquired by the *Clementine* spacecraft at a resolution of ~25 m/pixel (McEwen and Robinson, 1997; Robinson *et al.*, 2002b). Thus, no appropriate high-resolution data exist to test lunar regions of extended terminator crossings at the scale seen in the NEAR MSI images (better than 5 m/pixel). Electrostatic levitation could be less efficient on the Moon due to the much higher lunar gravity field (Cheng *et al.*, 2002).

Other workers have proposed that seismic shaking alone may result in formation of the ponds. So far these models do not adequately address the geographic distribution and color properties of the ponds, or the lack of "run out" features on the surfaces of the ponds or surrounding slopes (Cheng *et al.*, 2002). However they are formed, ponds show that complex processes exist on the asteroid that allow segregation and transport of regolith constituents to form sedimentary deposits having distinctive morphology, color,

TABLE 6. Color data presented in Fig. 23b (550/760 nm and 950/760 nm), locations shown in Fig. 22 top panel (top) or bottom panel (bottom).

Figure/Location	Label	550 avg	550 std	760 avg	760 std	950 avg	950 std	550/760	950/760	*n*
Fig. 22-Top	P-W	0.034	0.001	0.045	0.002	0.038	0.002	1.125	0.874	9
Fig. 22-Top	P-3	0.023	0.001	0.031	0.001	0.025	0.001	1.117	0.849	9
Fig. 22-Top	P-5	0.023	0.002	0.030	0.002	0.025	0.002	1.122	0.859	25
Fig. 22-Top	0.4° N-H	0.049	0.001	0.069	0.003	0.060	0.002	1.043	0.904	9
Fig. 22-Top	0.4° N-F	0.030	0.001	0.043	0.001	0.039	0.001	1.050	0.951	9
Fig. 22-Top	H0	0.067	0.003	0.093	0.004	0.082	0.004	1.060	0.932	121
Fig. 22-Top	H1	0.068	0.003	0.095	0.004	0.085	0.004	1.047	0.934	121
Fig. 22-Top	H2	0.064	0.002	0.091	0.003	0.082	0.003	1.044	0.942	121
Fig. 22-Top	4.2° S	0.062	0.003	0.088	0.005	0.075	0.004	1.045	0.897	49
Fig. 22-Top	4.2° S	0.030	0.003	0.043	0.003	0.043	0.003	1.042	1.049	49
Fig. 22-Top	X0	0.028	0.002	0.042	0.003	0.039	0.002	0.994	0.985	625
Fig. 22-Top	X1	0.045	0.002	0.067	0.003	0.063	0.002	0.991	0.989	625
Fig. 22-Top	X2	0.046	0.003	0.068	0.004	0.065	0.003	1.004	0.991	625
Fig. 22-Top	X3	0.037	0.002	0.054	0.003	0.052	0.003	0.996	1.007	625
Fig. 22-Top	X4	0.029	0.002	0.042	0.003	0.040	0.003	1.002	1.000	625
Fig. 22-Bottom	30.2° S	0.045	0.002	0.064	0.002	0.055	0.002	1.041	0.899	49
Fig. 22-Bottom	H3	0.051	0.002	0.071	0.003	0.060	0.003	1.069	0.896	49
Fig. 22-Bottom	H4	0.045	0.002	0.064	0.003	0.056	0.003	1.047	0.931	49
Fig. 22-Bottom	H5	0.045	0.003	0.064	0.003	0.058	0.002	1.054	0.952	49
Fig. 22-Bottom	X5	0.026	0.002	0.038	0.003	0.037	0.003	1.000	1.018	625
Fig. 22-Bottom	X6	0.022	0.002	0.033	0.003	0.031	0.003	1.001	1.006	625
Fig. 22-Bottom	X7	0.026	0.002	0.039	0.003	0.038	0.002	0.982	1.010	625

Ratios normalized to the median of the intercrater units "Xs", "Label" column indicates annotation in Fig. 22 locating sample area (P-W pond on upper wall, P-3 pond on lower wall with P-5 at same location but with 5 × 5 sample box).

and possibly geochemical (mineralogic?) properties. All evidence leads to the conclusion that ponds are composed of a relatively fine-grain fraction of the regolith that is mobilized and seeks gravitational lows while behaving as a fluid by some as yet undetermined process such as seismic shaking and/or electrostatic levitation (Veverka *et al.*, 2001a; Robinson *et al.*, 2001; Cheng *et al.*, 2002). Since the ponds are nearly crater free, relatively small, and probably consist of unconsolidated regolith they must be relatively young. They are probably being formed and erased on short timescales, and thus may imply a steady-state formation and destruction mechanism.

SUMMARY AND CONCLUSIONS

It is remarkable that on a small object such as Eros the three largest craters are so morphologically distinct from one another. Psyche is a classic bowl-shaped crater modified by downslope transport of finer components of the regolith. Shoemaker is a somewhat irregularly shaped depression surfaced with a poorly sorted layer of fragmental debris. Himeros exposes a variety of structural features (grooves, ridges, scarps) and hosts gravity driven flows more than a kilometer in length. All three show different morphologies indicating the efficacy of gravity driven processes in modifying the regolith on small bodies despite gravity <1 cm/s^2.

The NEAR MSI data (Fig. 24) show Eros has a pervasive regolith and clarify the early contradictory results of Earth-based thermal inertia estimates. Some indicated that a "lunar-like", highly porous regolith covered the asteroid (Morrison, 1976), while others (Lebofsky and Rieke, 1979) concluded that Eros was not "lunar-like" in that it most likely had on the order of 10–50% exposed bare rock (high thermal inertia). The terrain between Psyche, Shoemaker, and Himeros craters (Fig. 25) is notable for its lack of crater saturation at diameters below 100 to 200 m (Veverka *et al.*, 2000; Chapman *et al.*, 2002). Comparison to lunar and Phobos crater counts suggests this relative deficiency in small craters arises primarily due to preferential erasure of craters formed in a thick, loose, regolith.

Can we put global constraints on the depth of regolith? The fact that grooves, troughs and ridges are preserved on Eros requires a cohesive material at depth; such features could not form and be preserved if Eros were a completely comminuted, non-cohesive body (there must be coherent material at scales exceeding several 100 m at some depth). Because the Shoemaker crater impact event created an extensive boulder population (Thomas *et al.*, 2001), with sizes ranging up to 150 m, it must have excavated into a competent substrate some 200 to 300 m below the surface. Thus, at least in the area around Shoemaker crater, the regolith was no deeper than 200–300 m at the time of the impact. Numerous examples of partially buried craters indicate that at least 10–20 m of regolith is common

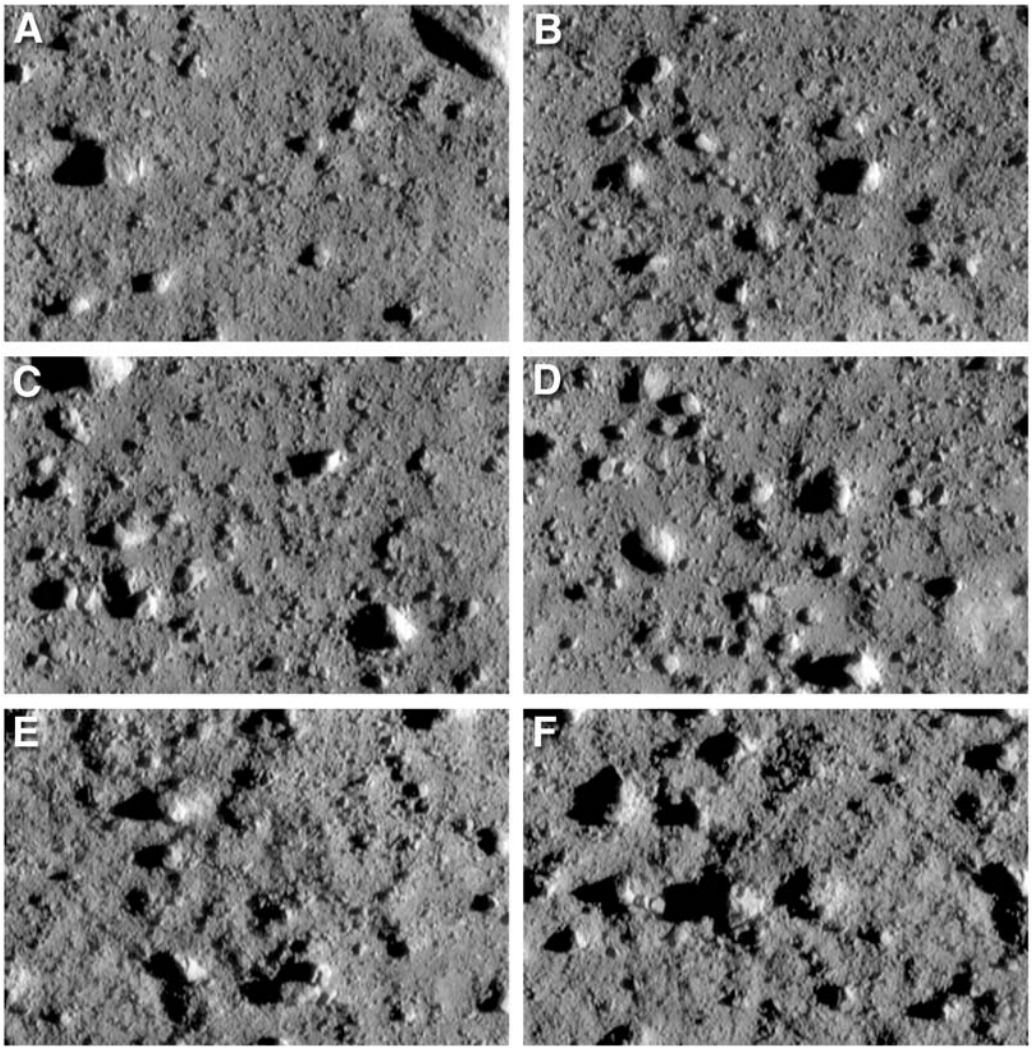

FIG. 24. During *NEAR Shoemaker's* descent to the surface extremely high-resolution imaging was obtained that reveals the regolith in great detail. Contrast the surface seen here with that in Shoemaker Regio shown in Fig. 11c at 10× coarser resolution (~3 m/pixel). (a) 157416918; width of frame ~36 m; (b) 157416938, width of frame ~35 m; (c) 157416983, width of frame ~33 m; (d) 157417003, width of frame ~31 m; (e) 157417048, width of frame ~27 m; (f) 157417068, width of frame ~25 m.

everywhere on the asteroid (*i.e.*, Fig. 10—many more examples exist than those shown in this paper).

Is there evidence of a similar pervasive regolith on other asteroids? The morphology of the pitted grooves and troughs seen on Eros is not as crisp and well defined as that observed on Phobos (Thomas *et al.*, 2000) indicating that the regolith on Eros is thicker than that on Phobos. In a comparison of the morphology of Deimos and Phobos Thomas *et al.* (1996) suggested that no fracture induced grooves are found on Deimos due to a global regolith depth exceeding 100–200 m, thus making it unlikely that fractures could remain morphologically distinguishable at the surface. Based on this interpretation the regolith on Eros is constrained to be <100 m, at least in areas of grooves. From much lower resolution *Galileo* flyby image data of Ida and Gaspra (31 m/pixel at best *vs.* 5 m/pixel global coverage of Eros) other hints of a regolith were found. Positive relief features (boulders) were identified on both Gaspra and Ida and most likely represent the extreme large end of a grain size distribution (cf., Carr *et al.*, 1994; Sullivan *et al.*, 1996). Depths of fresh craters on Ida and Gaspra were generally found to be lower than those for the Moon and Phobos (0.14–0.15 *vs.* 0.19–0.20); this condition was attributed to rapid degradation of original crater form due to formation in a regolith (Carr *et al.*, 1994; Sullivan *et al.*, 1996). Grooves on Ida were seen to have rounded or smoothed cross-sections indicating regolith depths equivalent to groove depths (≥10 m). On Gaspra small craters exhibiting circumferential ejecta deposits with relatively elevated visible and near-infrared color ratios (properties similar to Eros' ponds and higher reflectance crater wall deposits) were found on topographic ridges. Also on Gaspra it was noted that

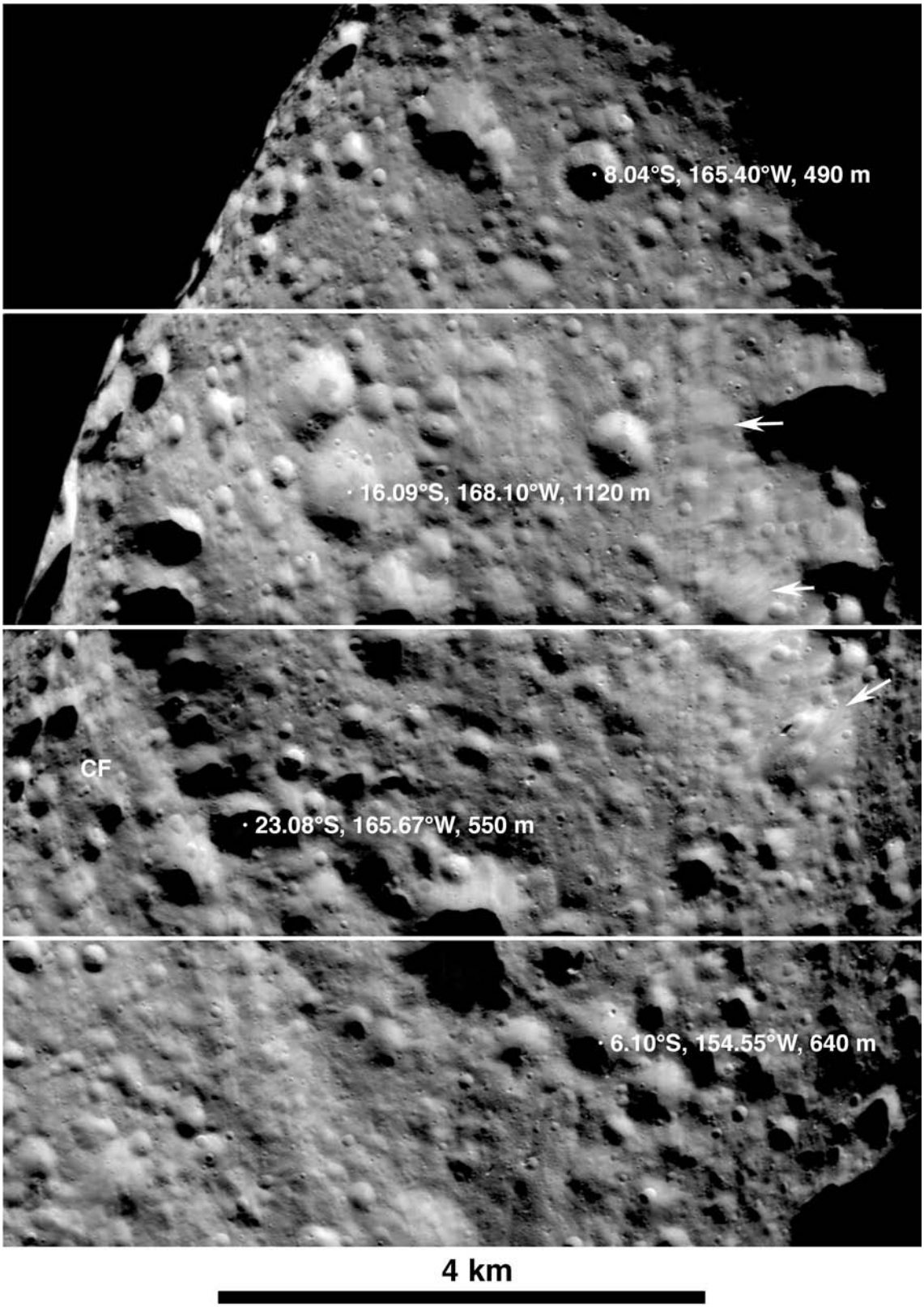

FIG. 25. Area west of crater Psyche free of obvious effects from large impacts. Subtle ridges and troughs making up Calisto Fossae (CF; Fig. 4) are visible on left. The many shoulder-to-shoulder craters have chiefly been modified by subsequent impacts through superposition and secondary crater impact. Various craters exhibit brighter reflectance materials on steeper slopes. Downslope movement of material is indicated by striated texture and smooth deposits (arrows). Boulders and small, crisp (fresh) craters appear randomly distributed and are relatively common. Where shadows inside craters are seen, their outlines are basically smooth curves, indicating a lack of layer discontinuities in crater walls (METs = 143504831–143505761).

some ridge crests also shared these same color properties; both units were interpreted to represent gravity-driven movement of regolith (Belton *et al.*, 1992; Carr *et al.*, 1994; Helfenstein *et al.*, 1994). The Ida and Gaspra results all point to the tentative interpretation that a substantial (≥10 m) regolith affects much of the physical properties and morphology of both asteroids and that remobilization influenced by gravity is a key process on asteroids. The NEAR results support these earlier interpretations—asteroid regoliths are substantial and gravity-driven processes result in a host of morphologies.

From our observations of Eros, and comparisons with other small bodies, it is likely that on average the regolith on Eros is loose to depths that may vary geographically, but are commonly 10–100 m. A lack of indicators of a strength boundary in the shallow subsurface (<50 m) further indicates that the regolith transitions from unconsolidated material to highly fractured semi-coherent material to a coherent substrate at some depth, and that a *well-defined* base or thickness of regolith may not exist on this object. A similar cross-sectional model for Eros was proposed by Wilkison *et al.* (2002) based on density–porosity arguments and for Ida from a host of observations (Sullivan *et al.*, 1996). Numerical simulations of impact damage on Ida are consistent with a thick regolith; a heavily brecciated (megaregolith) outer region transitioning to more coherent material at depth (Asphaug *et al.*, 1996).

The discovery of a global regolith on Eros has several important scientific implications for interpretation of remotely sensed spectral and geochemical properties. A pervasive mobile regolith (lacking any areally significant substrate outcrops) would result in a well-mixed homogenized surface layer, possibly masking any broad scale compositional heterogeneities inside Eros. Perhaps the lack of Ida-like broad-scale color units and Gaspra-like small crater color halos on Eros is a result of an even thicker or more mobile regolith than exists on either of these two bodies. As exemplified by ponds and higher albedo crater wall deposits, a whole new class of sedimentary processes has been discovered on Eros—low gravity sediment transport and sorting. Higher reflectance materials are found on steep slopes and commonly abruptly transition to lower reflectance materials, most likely at a break in slope. The pond surfaces are perpendicular to local gravity; these have spectral properties similar to the higher reflectance crater wall deposits but with a much smaller reflectance contrast. Synthesis of all available data demands that these features represent remobilization and grain separation of the regolith rather than rock type heterogeneities.

Operationally, a landing and sampling return mission to an asteroid with a regolith as extensive as that on Eros will require no drilling or chipping. Macroscopic material over a size range of at least 5 orders of magnitude should be readily available (subcentimeter to 100 m). Undoubtedly the majority of material that composes the surface is of subcentimeter scale grain size. A representative multi-kilogram sample of the whole asteroid could probably be obtained through scooping and plucking from a single, well-chosen landing site. The six frames shown in Fig. 24 have resolutions better than 12 cm/pixel, revealing a very blocky and poorly sorted surface. These images are of the interior upper rim of Himeros, with a regional slope of ~20°, and should be in area of net loss of regolith. The area covered by these frames most likely samples the ejecta blanket of the blocky crater (100 m diameter) in which *NEAR Shoemaker* landed. Here blocks greater than a half meter in diameter cover ~10% of the surface (Fig. 24d). Is this typical of Eros? Probably not; the previous 10 descent images (15–25 cm/pixel) show a much more benign surface, yet in each frame evidence of a poorly sorted regolith abounds. These final images show, as on the Moon, that the surface is generally accessible to a lander able to avoid rougher areas. The fact that *NEAR Shoemaker* successfully landed on the asteroid (Veverka *et al.*, 2001b) despite the fact that it was designed as an orbiter and not a lander (no landing gear or hazard avoidance capability) testifies not only to the competence of the NEAR Operations Team but to the hospitality of the surface.

Acknowledgments–We thank Paul Spudis, Mary Ann Hager, and the professional staff at the Lunar and Planetary Institute for providing ready access to high-resolution Lunar Orbiter images and supporting materials. The NEAR image sequencing team led by A. Harch (Cornell University) relentlessly planned spacecraft command loads on a weekly basis over the course of a year to obtain the data that made this study possible. The Jet Propulsion Laboratory Navigation Team provided timely ephemeris updates on an ongoing basis during the mission that allowed extremely accurate targeting, an enormous task that often goes unrecognized. The Johns Hopkins University Applied Physics Laboratory (APL) Mission Operations and Management Teams led by T. Coughlin and B. Farquhar made one of the most amazing success stories in the history of unmanned solar system exploration seem simple; without their dedication to maximizing the science return of the mission many of the discoveries outlined in this paper would never have been made. We are grateful to E. Asphaug and D. Britt for providing reviews. NASA supported this work through the NEAR Data Analysis Program (NDAP).

Editorial handling: D. W. G. Sears

REFERENCES

ACKERMANN H. D., GOODSON R. H. AND WATKINS J. S. (1975) A seismic refraction technique used for subsurface investigations at Meteor Crater, Arizona. *J. Geophys. Res.* **80**, 765–775.

ACUÑA M. H., ANDERSON B. J., RUSSELL C. T., WASILEWSKI P., KLETETSHKA G., ZANETTI L. AND OMIDI N. (2002) NEAR magnetic field observations at 433 Eros: First measurements from the surface of an asteroid. *Icarus* **155**, 220–228.

ADAMS J. B. AND FILICE A. L. (1967) Spectral reflectance 0.4 to 2.0 microns of silicate rock powders. *J. Geophys. Res.* **72**, 5705–5715.

ARNOLD J. R. (1979) Ice in the lunar poles. *J. Geophys. Res.* **84**, 5659–5668.

ARVIDSON R., CROZAZ G., DROZD R. J., HOHENBERG C. M. AND MORGAN C. J. (1975) Cosmic ray exposure ages of the features and events at the Apollo landing sites. *The Moon* **13**, 67–69.

ASPHAUG E. AND MELOSH H. J. (1993) The Stickney impact of Phobos: A dynamical model. *Icarus* **101**, 144–164.

ASPHAUG E., MOORE J. M., MORRISON D., BENZ W., NOLAN M. C. AND SULLIVAN R. J. (1996) Mechanical and geologic effects of impact cratering on Ida. *Icarus* **120**, 158–184.

BARNOUIN-JHA O. *ET AL.* (2000) Characterizing the regolith of asteroid 433 Eros from laser altimetry and imaging (abstract). *EOS, Trans. Am. Geophys. Union* **81**, F805.

BELL J. F. (2001) Eros: A comprehensive model (abstract). *Lunar Planet. Sci.* **32**, #1964, Lunar and Planetary Institute, Houston, Texas, USA (CD-ROM).

BELL J. F., DAVIS D. R., HARTMANN W. K. AND GAFFEY M. J. (1989) Asteroids: The big picture. In *Asteroids II* (eds. R. P. Binzel, T. Gehrels and M. S. Matthews). Univ. Arizona Press, Tucson, Arizona, USA.

BELL J. F., III *ET AL.* (2002) Near-IR reflectance spectroscopy of 433 Eros from the NIS instrument on the NEAR mission. *Icarus* **155**, 119–144.

BELTON M. J. S. *ET AL.* (1992) *Galileo* encounter with 951 Gaspra: First pictures of an asteroid. *Science* **257**, 1647–1652.

BERTHOUD M., THOMAS P. AND VEVERKA J. (2001) Eros crater densities in 3 major impact features (abstract). *Bull. Am. Astron. Soc.* **33**, 1149.

BINZEL R. P., GEHRELS T. AND MATTHEWS M. S., EDS. (1989) *Asteroids II.* Univ. Arizona Press, Tucson, Arizona, USA. 1258 pp.

BUNCH T. E. AND RAJAN R. S. (1988) Meteorite regolithic breccias. In *Meteorites and the Early Solar System* (eds. J. F. Kerridge and M. S. Matthews), pp. 144–164. Univ. Arizona Press, Tucson, Arizona, USA.

BUSSEY D. B. J., SPUDIS P. D. AND ROBINSON M. S. (1999) Illumination conditions at the lunar south pole. *Geophys. Res. Lett.* **26**, 1187–1190.

BUSSEY D. B. J., ROBINSON M. S., EDWARDS K., THOMAS P. C., JOSEPH J., MURCHIE S., VEVERKA J. AND HARCH A. P. (2002) 433 Eros global basemap from NEAR Shoemaker images. *Icarus* **155**, 38–50.

CARR M. H., KIRK R., MCEWEN A., VEVERKA J., THOMAS P. C., HEAD J. AND MURCHIE S. (1994) The geology of Gaspra. *Icarus* **107**, 61–71.

CHAPMAN C. R., MERLINE W. J., THOMAS P. C., JOSEPH J., CHENG A. F. AND IZENBERG N. (2002) Impact history of Eros: Craters and boulders. *Icarus* **155**, 104–118.

CHAPPELOW J. E. AND SHARPTON V. L. (2002) An improved shadow measurement technique for constraining the morphometry of simple impact craters. *Meteorit. Planet. Sci.* **37**, 479–486.

CHENG A. F. *ET AL.* (2001) Laser altimetry of small-scale features on 433 Eros from NEAR-Shoemaker. *Science* **292**, 488–491.

CHENG A. F., IZENBERG N., CHAPMAN C. R. AND ZUBER M. T. (2002) Ponded deposits on Eros. *Meteorit. Planet. Sci.* **37**, 1095–1105.

CINTALA M. J. AND MCBRIDE K. M. (1995) Block distribution on the lunar surface: A comparison between measurements obtained from surface and orbital photography. NASA Technical memorandum **104804**, NASA, Johnson Space Center, Houston, Texas, USA. 441 pp.

CINTALA M. J., HEAD J. W. AND VEVERKA J. (1978) Characteristics of the cratering process on small satellites and asteroids. *Proc. Lunar Planet. Sci. Conf.* **9th**, 3803–3830.

CINTALA M. J., HEAD J. W. AND WILSON L. (1979) The nature and effects of impact cratering on small bodies. In *Asteroids* (ed. T. Gehrels), pp. 579–600. Univ. Arizona Press, Tucson, Arizona, USA.

CLARK B. E. *ET AL.* (2001) Space weathering on Eros: Constraints from albedo and spectral measurements of Psyche crater. *Meteorit Planet. Sci.* **36**, 1617–1637.

CLARK B. E., HELFENSTEIN P., BELL J. F., III, PETERSON C., VEVERKA J., IZENBERG N. I., DOMINGUE D., WELLNITZ D. AND MCFADDEN L. (2002) Near infrared spectrometer photometry of asteroid 433 Eros. *Icarus* **155**, 189–204.

COLLINS G. C. (2000) Driving mechanisms for grooved terrain tectonics on Ganymede and chaotic terrain formation on Europa: Constraints from Galileo data. Ph.D. thesis, Brown University, Providence, Rhode Island, USA. 204 pp.

CRATER ANALYSIS TECHNIQUES WORKING GROUP (1979) Standard techniques for presentation and analysis of crater size frequency data. *Icarus* **37**, 467–474.

CROZAZ G., WALKER R. AND WOOLUM D. (1971) Nuclear track studies of dynamic surface processes on the Moon and constancy of solar activity. *Proc. Lunar Sci. Conf.* **2nd**, 2543–2558.

DIETRICH J. W. AND CLANTON U. S. (1972) 4. Photographic summary. In *Apollo 16 Preliminary Science Report.* pp. 4-1 to 4-32. NASA SP-**315**, Washington D.C., USA.

DOMINGUE D. L., ROBINSON M., CARCICH B., JOSEPH J., THOMAS P. AND CLARK B. E. (2002) Disk-integrated photometry of 433 Eros. *Icarus* **155**, 205–219.

EVANS L. G., STARR R. D., BRÜCKNER J., REEDY R. C., BOYNTON W. V., TROMBKA J. I., GOLDSTEIN J. O., MASARIK J., NITTLER L. R. AND MCCOY T. J. (2001) Elemental composition from gamma-ray spectroscopy of the NEAR–Shoemaker landing site on 433 Eros. *Meteorit. Planet. Sci.* **36**, 1639–1660.

GEISSLER P., PETIT J-M., DURDA D., GREENBERG R., BOTTKE W., NOLAN M. AND MOORE J. (1996) Erosions and ejecta reaccretion on 243 Ida and its moon. *Icarus* **120**, 140–157.

GRADIE J. AND VEVERKA J. (1986) The wavelength dependence of phase coefficients. *Icarus* **66**, 455–467.

GRADIE J., VEVERKA J. AND BURATTI B. (1980) The effects of scattering geometry on the spectrophotometric properties of powdered material. *Proc. Lunar Planet. Sci. Conf.* **11th**, 799–815.

GREENBERG R., BOTTKE W., NOLAN M., GEISSLER P., PETIT J. M., DURDA D., ASPHAUG E. AND HEAD J. (1996) Collisional and dynamical history of Ida. *Icarus* **120**, 106–118.

HAPKE B. (2001) Space weathering from Mercury to the asteroid belt. *J. Geophys. Res.* **106**, 10 039–10 073.

HAWKINS S .E., III *ET AL.* (1997) Multi-spectral imager on the Near Earth Asteroid Rendezvous Mission. *Space Sci. Rev.* **82**, 31–100.

HEIKEN G. H., VANIMAN D. T. AND FRENCH B. M. (1991) *Lunar Sourcebook.* Cambridge Univ. Press, New York, New York, USA. 736 pp.

HELFENSTEIN P. *ET AL.* (1994) Galileo photometry of asteroid 951 Gaspra. *Icarus* **107**, 37–60.

HORSTMAN K. C. AND MELOSH H. J. (1989) Drainage pits in cohesionless materials: Implications for the surface of Phobos. *J. Geophys. Res.* **94**, 12 433–12 441.

HOWARD K. A. AND LARSEN B. A. (1972) Lineaments that are artifacts of lighting. In *Apollo 15 Preliminary Science Report.* pp. 25-58 to 25-63. NASA SP **289**, NASA, Washington D.C., USA.

KEIL K. (1982) Composition and origin of chondritic breccias. In *Workshop on Lunar Breccias and Soils and their Meteoritic Analogs* (eds. G. J. Taylor and L.L. Wilkening), pp. 65–83. LPI Tech. Report **83-02**, Lunar and Planetary Institute, Houston, Texas, USA.

KERRIDGE J. F. AND MATTHEWS M. S., EDS. (1988) *Meteorites and the Early Solar System.* Univ. Arizona Press, Tucson, Arizona, USA. 1269 pp.

LEBOFSKY L. A. AND RIEKE G. H. (1979) Thermal properties of 433 Eros. *Icarus* **40**, 297–308.

LEE P. (1996) Dust levitation on asteroids. *Icarus* **124**, 181–194.

LI H., ROBINSON M. S. AND MURCHIE S. L. (2002) Preliminary remediation of scattered light in NEAR MSI images. *Icarus* **155**, 244–252.

LISSAUER J. J., SQUYRES S. W. AND HARTMANN W. K. (1988) Bombardment history of the Saturn system. *J. Geophys. Res.* **93**, 13 776–13 804.

LUCEY P. G., HINRICHS J. L., URQUHART M., WELLNITZ D., IZENBERG N. I., MURCHIE S., ROBINSON M. S., CLARK B. E. AND BELL J. F., III (2002) Detection of temperature-dependent spectral variation on

the asteroid Eros and new evidence for the presence of an olivine-rich silicate assemblage. *Icarus* **155**, 181–188.

LUCCHITTA B. K. (1972) Geologic map of part of the Taurus-Littrow region of the Moon Apollo 17 pre-mission map. USGS Map I-800, 1:50,000. U. S. Geologic Survey, Washington, D.C., USA.

MATSON D. L., JOHNSON T. V. AND VEEDER G. J. (1977) Soil maturity and planetary regoliths: The Moon, Mercury, and the asteroids. *Proc. Lunar Sci. Conf.* **8**, 1001–1011.

MCCORD T. B. AND JOHNSON T. V. (1970) Lunar spectral reflectivity (0.30 to 2.50 microns) and implications for remote mineralogical analysis. *Science* **169**, 855–858.

MCCORD T. B. AND ADAMS J. B. (1973) Progress in remote optical analysis of lunar surface composition. *Moon* **7**, 453–474.

MCCOY T. J. *ET AL.* (2001) The composition of 433 Eros: A mineralogical–chemical synthesis. *Meteorit. Planet. Sci.* **36**, 1661–1672.

MCCOY T. J., ROBINSON M. S., NITTLER L. R. AND BURBINE T. H. (2002) The Near-Earth Asteroid mission to asteroid 433 Eros: A milestone in the study of asteroids and their relationship to meteorites. *Chem. Erde* **62**, 89–121.

MCEWEN A. S. AND ROBINSON M. S. (1997) Mapping of the Moon by Clementine. *Adv. Space Res.* **19**, 1523–1533.

MITCHELL D. L., HUDSON R. S., OSTRO S. J. AND ROSEMA K. D. (1998) Shape of asteroid 433 Eros from inversion of Goldstone radar doppler spectra. *Icarus* **131**, 4–14.

MOORE H. J. (1964) Density of small craters on the lunar surface. In *Astrogeologic Studies Annual Progress Report, August 1962–July 1963, Part D.*, pp. 34–51. U. S. Geological Survey, Washington, D.C., USA.

MORRISON D. (1976) The diameter and thermal inertia of 433 Eros. *Icarus* **28**, 125–132.

MURCHIE S. L. *ET AL.* (1999) Inflight calibration of the NEAR multispectral imager. *Icarus* **140**, 66–91.

MURCHIE S., ROBINSON M., DOMINGUE D., LI H., PROCKTER L., HAWKINS S. E., III, OWEN W., CLARK B. AND IZENBERG N. (2002a) Inflight calibration of the NEAR multispectral imager, 2: Results from Eros approach and orbit. *Icarus* **155**, 229–243.

MURCHIE S. L. *ET AL.* (2002b) Color variations on Eros from NEAR multispectral imaging. *Icarus* **155**, 145–168.

NITTLER L. R. *ET AL.* (2001) X-ray fluorescence measurements of the surface elemental composition of asteroid 433 Eros. *Meteorit. Planet. Sci.* **36**, 1673–1695.

OBERBECK V. R. AND QUAIDE W. L. (1967) Estimated thickness of a fragmental surface layer of Oceanus Procellarum. *J. Geophys. Res.* **72**, 4697–4704.

OBERBECK V. R. AND QUAIDE W. L (1968) Genetic implications of lunar regolith thickness variations. *Icarus* **9**, 446–465.

PIETERS C. M., TAYLOR L. A., NOBLE S. K., KELLER L. P., HAPKE B., MORRIS R. V., ALLEN C. C., MCKAY D. S. AND WENTWORTH S. (2001) Space weathering on airless bodies: Resolving a mystery with lunar samples. *Meteorit. Planet. Sci.* **35**, 1101–1107.

PIKE R. J. (1977) Size dependence in the shape of fresh impact craters on the Moon. In *Impact and Explosion Cratering* (eds. D. J. Roddy, R. O. Pepin and R. B. Merrill), pp. 489–509. Pergamon, New York, New York, USA.

PROCKTER L. M. *ET AL.* (2002) Surface expressions of structural features on Eros. *Icarus* **155**, 75–93.

QUAIDE W. L. AND OBERBECK V. R. (1968) Thickness determinations of the lunar surface layer from lunar impact craters. *J. Geophys. Res.* **73**, 5247–5270.

ROBINSON M. S. AND JOLLIFF B. L. (2002) *Apollo 17* landing site: Topography, photometry, and heterogeneity of the highland massifs. *J. Geophys. Res.* (in press).

ROBINSON M. S., THOMAS P. C., VEVERKA J., MURCHIE S. L. AND CARCICH B. (2001) The nature of ponded deposits on Eros. *Nature* **413**, 396–400.

ROBINSON M. S. *ET AL.* (2002a) NEAR MSI mosaics of 433 Eros (abstract). *Lunar Planet. Sci.* **33**, #1671, Lunar and Planetary Institute, Houston, Texas, USA (CD-ROM).

ROBINSON M. S., MALARET E. AND WHITE T. (2002b) A calibration for the Clementine HIRES camera. *J. Geophys. Res.* (in press).

SCHULZ P. H. AND GAULT D. E. (1975) Seismically induced modification of lunar surface features. *Proc. Lunar Sci. Conf.* **6th**, *Geochim. Cosmochim. Acta* **6 (Suppl.)**, 2845–2862.

SHOEMAKER E. M. (1966a) Preliminary analysis of the fine structure of the lunar surface in Mare Cognitum. In *The Nature of the Lunar Surface* (eds. W. N. Hess, D. H. Menzel and J. A. O'Keefe), pp. 23–78. Johns Hopkins Univ. Press, Baltimore, Maryland, USA.

SHOEMAKER E. M. (1966b) Progress in the analysis of fine structure and geology of the lunar surface from the Ranger VIII and IX photographs. In *Ranger VIII and IX. Part II. Experimenters' Analyses and Interpretations* (eds. R. L. Heacock, G. P. Kuiper, E. M. Shoemaker, H. C. Urey and E. A. Whitaker), pp. 249–337. JPL Technical Report **32-800**, Jet Propulsion Laboratory, Pasadena, California, USA.

SHOEMAKER E. M. AND MORRIS E. C. (1968) Thickness of the regolith. In *Surveyor Project Final Report Part II. Science Results*, pp. 102–103. JPL Technical Report **32-1265**, Jet Propulsion Laboratory, Pasadena, California, USA.

SHOEMAKER E. M., BATSON R. M., HOLT H. E., MORRIS E. C., RENNILSON J. J. AND WHITAKER E. A. (1968) Television observations from Surveyor VII. In *Surveyor VII: A Preliminary Report*, pp. 13–81. NASA SP-166, NASA, Washington, D.C., USA.

SODERBLOM L. A. (1970) A model for small impact erosion applied to the lunar surface. *J. Geophys Res.* **75**, 2655–2661.

SULLIVAN R. *ET AL.* (1996) Geology of 243 Ida. *Icarus* **120**, 119–139.

THOMAS P. (1979) Surface features of Phobos and Deimos. *Icarus* **40**, 223–243.

THOMAS P. C. (1998) Ejecta emplacement on the martian satellites. *Icarus* **131**, 78–106.

THOMAS P. C. (1999) Large craters on small objects: Occurrence, morphology, and effects. *Icarus* **142**, 89–96.

THOMAS P., ADINOLFI D., HELFENSTEIN P., SIMONELLI D. AND VEVERKA J. (1996) The surface of Deimos: Contribution of materials and processes to its unique appearance. *Icarus* **123**, 536–556.

THOMAS P. C. *ET AL.* (1999) Mathilde, size, shape, and geology. *Icarus* **140**, 17–27.

THOMAS P. C., VEVERKA J., SULLIVAN R., SIMONELLI D. P., MALIN M. C., CAPLINGER M., HARTMANN W. K. AND JAMES P. B. (2000) Phobos: Regolith and ejecta blocks investigated with Mars orbiter camera images. *J. Geophys. Res.* **105**, 15 091–15 106.

THOMAS P. C., VEVERKA J., ROBINSON M. S. AND MURCHIE S. L. (2001) Shoemaker crater: A major source of ejecta on asteroid 433 Eros. *Nature* **413**, 394–396.

THOMAS P. C., JOSEPH J., ROBINSON M., MURCHIE S., VEVERKA J., CLARK B. E. AND CHAPMAN C. (2002a) Shape, slopes, and slope processes on Eros. *Icarus* **155**, 18–37.

THOMAS P. C., PROCKTER L., ROBINSON M., JOSEPH J. AND VEVERKA J. (2002b) Global structure of asteroid 433 Eros. *Geophys. Res. Lett.*, 10.1029/2001GL014599.

TRASK N. J. (1969) *Geologic maps of early Apollo landing sites, explanatory pamphlet accompanying USGS Maps I-616 through I-627.* US Geologic Survey, Washington, D.C., USA. 4 pp.

TRASK N. J. (1971) Geologic comparison of mare materials in the lunar equatorial belt, including Apollo 11 and Apollo 12 landing sites. In *Geological Survey Research*, pp. D138–D144. USGS

Professional Paper, **750-D**, US Geologic Survey, Washington, D.C., USA.

TRASK N. J. AND ROWAN L. C. (1967) Lunar Orbiter photographs: Some fundamental observations. *Science* **158**, 1529–1535.

TROMBKA J. I. *ET AL.* (2001) The NEAR Shoemaker x-ray/gamma-ray spectrometer experiment: Overview and lessons learned. *Meteorit. Planet. Sci.* **36**, 1605–1616.

VEVERKA J. *ET AL.* (1997a) NEAR's flyby of 253 Mathilde: Images of a C asteroid. *Science* **278**, 2109–2114.

VEVERKA J. *ET AL.* (1997b) An overview of the NEAR multispectral imager (MSI)—Near infrared spectrometer (NIS) investigation. *J. Geophys. Res.* **102**, 23 709–23 728.

VEVERKA J. *ET AL.* (1999) Imaging of asteroid 433 Eros during NEAR's flyby reconnaissance. *Science* **285**, 562–564.

VEVERKA J. *ET AL.* (2000) NEAR at Eros: Imaging and spectral results. *Science* **289**, 2088–2097.

VEVERKA J. *ET AL.* (2001a) Imaging of small-scale features on 433 Eros from NEAR: Evidence for a complex regolith. *Science* **292**, 484–488.

VEVERKA J. *ET AL.* (2001b) NEAR Shoemaker's descent to Eros: Unexpected depositional and erosional features in the regolith. *Nature* **413**, 390–393.

WAHL W. (1952) The brecciated stoney meteorites and meteorites containing foreign fragments. *Geochim. Cosmochim. Acta* **2**, 91–117.

WILCOX B., ROBINSON M. S. AND THOMAS P. (2002) Regolith thickness, distribution, and processes examined at sub-meter resolution (abstract). *Workshop on Moon Beyond 2002* #3048, Lunar and Planetary Institute, Houston, Texas, USA (CD-ROM).

WILHELMS D. E. (1987) *The Geologic History of the Moon.* U.S. Geological Survey Prof. Paper **1348**, U. S. Geologic Survey, Washington, D.C., USA. 302 pp.

WILKISON S. L., ROBINSON M. S., THOMAS P. C., VEVERKA J., MCCOY T. J., MURCHIE S. L., PROCKTER L. AND YEOMANS D. (2002) An estimate of Eros' porosity and implications for internal structure. *Icarus* **155**, 94–103.

YOUNG J. W., MATTINGLY T. K. AND DUKE C. M. (1972) 5. Crew observations. In *Apollo 16 Preliminary Science Report*, pp. 5-1 to 5-6. NASA SP-315, Washington, D.C., USA.

ZUBER M. T. *ET AL.* (2000) The shape of 433 Eros from NEAR Shoemaker laser rangefinder. *Science* **289**, 2097–2101.